

# **CALSPAN-UB**

## **RESEARCH CENTER**



PLEASE RETURN TO:

BMD TECHNICAL INFORMATION CENTER  
BALLISTIC MISSILE DEFENSE ORGANIZATION  
7100 DEFENSE PENTAGON  
WASHINGTON D.C. 20301-7100

DTIC QUALITY INSPECTED 4

---

CALSPAN-UB RESEARCH CENTER

19980309 108

U5690

# **CALSPAN-UB**

## **RESEARCH CENTER**

### **Large Energy National Shock Tunnel (LENS)**

**DESCRIPTION AND CAPABILITES**

PLEASE RETURN TO:

BMD TECHNICAL INFORMATION CENTER  
BALLISTIC MISSILE DEFENSE ORGANIZATION  
7100 DEFENSE PENTAGON  
WASHINGTON D.C. 20301-7100

**DTIC QUALITY INSPECTED 4**

---

CALSPAN-UB RESEARCH CENTER

19980309 108

U5690



# Large Energy National Shock Tunnel (LENS)

DESCRIPTION AND CAPABILITES

DECEMBER 1990

**DISTRIBUTION STATEMENT A**  
Approved for public release;  
Distribution Unlimited

Accession Number: 5690

Publication Date: Dec 01, 1990

Title: Large Energy National Shock Tunnel (LENS)

Corporate Author Or Publisher: Calspan-UP Research Center, PO Box 400, Buffalo, NY 14225

Descriptors, Keywords: Energy National Shock Tunnel LENS

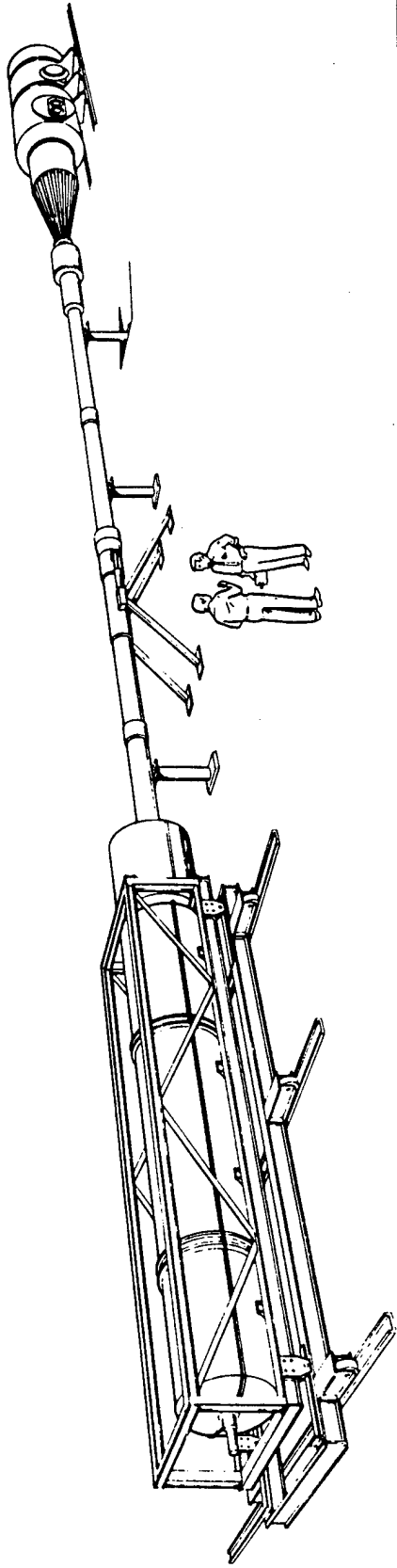
Pages: 00058

Cataloged Date: May 25, 1995

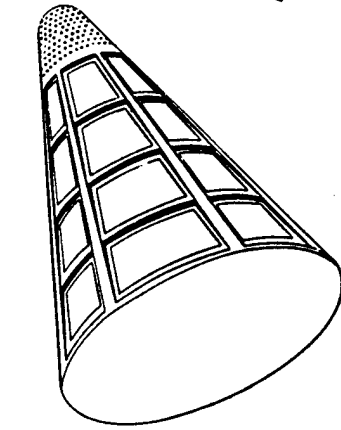
Document Type: HC

Number of Copies In Library: 000001

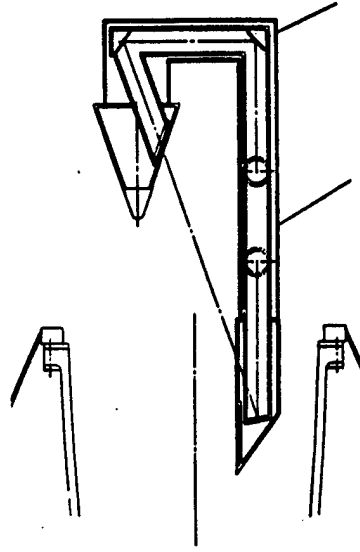
Record ID: 30053



1



VALIDATED TEST FACILITY AND  
AERO-OPTIC INSTRUMENTATION FOR  
SEEKER HEAD EVALUATION



VALIDATED AERO-OPTIC APERTURE EVALUATION CAPABILITY

## Table of Contents

	Page
Foreword .....	3
Introduction .....	4
Summary of Facility Capabilities .....	5
Program Costs and Schedules .....	6
Facility Description .....	7
Shock Tunnel Operating Principles .....	9
Detailed Operating Characteristics .....	11
Non-Conventional Testing .....	22
General Airflow Data and Calibration .....	24
Instrumentation .....	26
Aero-Optical Measurements of Seeker Head Performance .....	45
Data Acquisition and Processing System .....	51
Model Design and Fabrication .....	52
Model Support and Optical Bench System .....	54
References .....	56

## FOREWORD

The Calspan/University at Buffalo Research Center (CUBRC) Large Energy National Shock Tunnel (LENS) is high-enthalpy facility constructed to provide duplication of flight velocities in the range from 6000 to 14,000 ft/sec at typical re-entry altitudes, satisfying a requirement for the experimental study of turbulent compressible flows and real gas chemistry in hypervelocity flows. The design of this facility was based on our extensive and successful experience with the 48- and 96-inch shock tunnels at Calspan. These facilities have been used extensively in fundamental research and testing programs in hypersonic flow and include:

- detailed surface and flowfield measurements in laminar and turbulent regions of shock wave-boundary layer interaction for code validation (see page 40),
- studies of window cooling with film and transpiration cooling techniques (see reference 34),
- refraction and dispersion of light by shock waves and turbulent viscous layers (see reference 32),
- microwave-plasma interaction studies (see reference 9),
- SCRAMJET performance studies including hydrogen/air mixing and combustion under flight duplicated conditions in hypersonic flow (see Reference 39),
- force, moment, pressure, heat transfer and skin friction measurements as well as flowfield surveys on simple and complex hypersonic vehicle configurations (see References 28, 29, 30).

Routine shock tunnel studies have been conducted since the 48-inch shock tunnel came on line in 1959. Air is generally used as the test gas, however, other atmospheres can be simulated by loading the driven tube with the appropriate gases and performing the correct driver gas selection.

When the tunnel and aero-optic instrumentation have been checked out and calibrated the LENS facility will be operated by CUBRC as a government test facility for the aero-optical evaluation and development of seeker head apertures.

In the following sections we describe the operational characteristics of the LENS facility based on data generated in the operation of the 48- and 96-inch shock tunnels at Calspan. The operating charts, model and flowfield instrumentation, and test section and sting information can be used for preliminary design purposes. However, tunnel conditions, model and instrumentation for a specific experimental program should be discussed with members of the CUBRC staff. For detailed information on the operation of this facility please address your questions to:

Dr. Michael S. Holden  
Calspan/University of Buffalo Research Center (CUBRC)  
P.O. Box 400  
Buffalo, New York 14225

Telephone: 716-631-6853

## INTRODUCTION

Calspan Corporation has been active since 1950 in the application of the basic shock tube to a hypersonic test facility, overcoming the pressure and temperature limitations of the conventional hypersonic test facility. The primary shortcoming of the shock tunnel as a hypersonic test apparatus was the brief testing time available. In 1957, however, the *tailored-interface* modification was perfected, which increased the test time by a factor of approximately eight over that of a conventional non-reflected shock tunnel. This increase in running time effectively extended the potential of the shock tunnel beyond that of a company apparatus, suitable for the investigation of the physics of high-pressure, high-temperature gases, to that of a facility capable of providing detailed aerodynamic and aerothermodynamic design data.

In 1958, an 11x15-inch shock tunnel was made available to outside organizations for basic research investigations and for developmental testing of new designs. Acceptance of this tunnel by industry and advances in instrumentation led Calspan to construct a larger tunnel designed specifically for development testing. The 48-inch Hypersonic Shock Tunnel was placed in operation on July 1, 1959. With the modification of the facility to the high-energy facility, designated the 96-inch (high energy) leg, in January 1964, a considerable increase in performance over that previously available was achieved.

In 1983 a new not-for-profit research institute, the Calspan/University at Buffalo Research Center (CUBRC) was formed to exploit the combined talents of the two organizations to perform fundamental research, including hypersonic flows. As the result of an assessment by CUBRC of the state-of-the-art in experimental research, an effort was initiated to design a new facility which would address problems associated with turbulent compressible flows, non-equilibrium air chemistry and combustion in the velocity range from 6000 to 14,000 ft/sec. In 1987 this design activity was supported by a grant from NASA, and the funds for construction of the driver section of the tunnel were received from Air Force Office of Science Research (AFOSR) in 1989. The facility will be completed under a contract with AFOSR in 1991 and operated as a government furnished facility in support of the seeker head evaluation program beginning in 1992.

## SUMMARY OF FACILITY CAPABILITIES

The performance capabilities of the tunnel are summarized in the following table. The extreme values listed in this table relate to specific conditions of operation and are not to be interrelated without reference to the detailed operating characteristics presented on pages 9 through 21.

RANGES OF TUNNEL PERFORMANCE FOR LENS FACILITY				
Nozzle Exit Diameter (Inches)	Test Mach Number	Reynolds Number Per Foot	Test Air Supply Pressure (psia)	Test Air Supply Temp. (°R)
24 Contoured	6.5-8.2	$5.5 \times 10^4 - 1.6 \times 10^8$	5000-20,000	1300-11,500
48 Contoured	1.0-22	$1.7 \times 10^3 - 2.8 \times 10^7$	500-30,000	1900-14,000

## PROGRAM COSTS AND SCHEDULES

During the seeker head evaluation program CUBRC will operate LENS as a government furnished facility. Costs are estimated based on a detailed review of each customer's specific requirements and reflected the type of program, number of runs, number of model installations and changes, the amount and type of instrumentation and the number of data channels to be recorded.

The cost of a test program may be looked at as having two parts; fixed and variable. Both are dependent on the type of program. The fixed cost consists of pretest engineering, instrumentation, model installation and reporting. The variable cost, which is dependent on the number of runs as well as the type program, consists of labor costs to operate the facility, gases, diaphragms and data reduction and analysis. There is no hourly occupancy charge. Model design and fabrication costs are considered separately because of the wide variation in costs dependent upon model complexity and the desire of some customers to handle part or all of this task themselves. CUBRC has facilities for these functions (see page 52), but is willing to work in a manner most convenient to the customer.

### Data Acquisition

Runs per 8-hour shift for routine tests	1 to 3
Number of shifts per week	5 to 9
Model recording channels per run*	128 to 240

### Schedule

Test programs are generally scheduled within three to six months after receipt of contract. Preliminary data are available within two weeks after a test, and the final data report is issued within 90 days after completion of tests.

---

\*Additional channels are available if required.

## FACILITY DESCRIPTION

### Large Energy National Shock Tunnel (LENS)

The basic components of the LENS facility are shown in Figure 1. The driver/driven configuration consists of a chambered shock tube with an area ratio (driver/driven) of 2. The 11.5-inch internal diameter driver is 25 feet long and is externally heated by a resistance heater to 1260°R. The 8-inch internal diameter driven tube is 50 feet long. A hydrogen-nitrogen or helium-air mixture is used as the driver gas. Air is generally the driven gas, although other gases may be used. The tailored-interface mode of operation is used to provide the longest possible steady-state reservoir conditions. Maximum driver pressure is 30,000 psi, which yields a maximum pressure behind the reflected shock of 30,000 psi.

Four axisymmetric nozzles are available:

Nozzle	Type	Exit Diameter in Inches	Test Section Mach Number
A	Contoured	24	6.5 to 8.2
D	Contoured	48	10 to 17
E	10 $\frac{1}{2}$ ° Semi-angle cone	48	7 to 22
F	10 $\frac{1}{2}$ ° Semi-angle cone	72	8.6 to 24

The contoured nozzles provide parallel flow with no pressure gradients in the streamwise direction for several feet. We do not recommend the use of conical nozzles because the presence of a streamwise pressure gradient can have a significant effect on model test results. The nozzles employ replaceable throat inserts of different diameters so that, with the particular nozzle, the test Mach number can be varied. Test air passes through the test section into a receiver tank of a size sufficient to maintain the desired flow for durations of 2 to 27 milliseconds. All nozzles are calibrated using pitot-pressure survey rakes over the Mach number range indicated.

---

\*The shock tunnel is adaptable to the study of hypersonic flight in other planetary atmospheres.

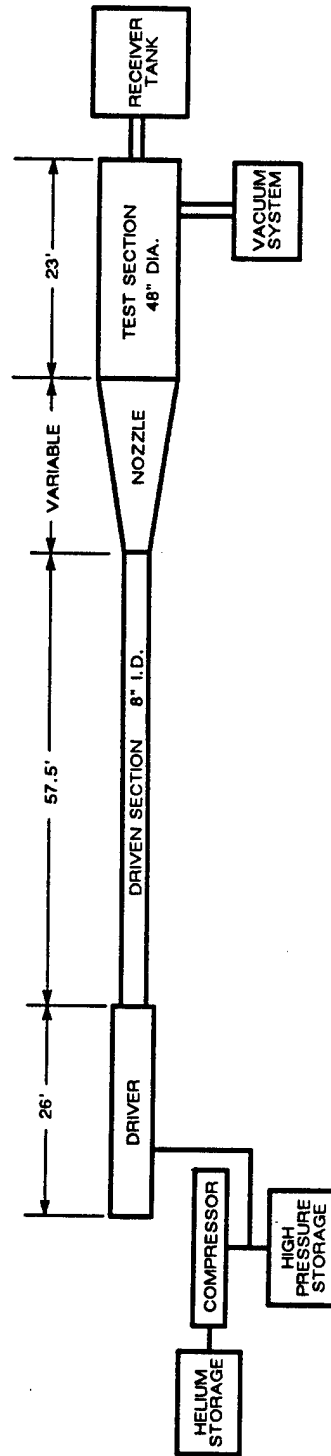
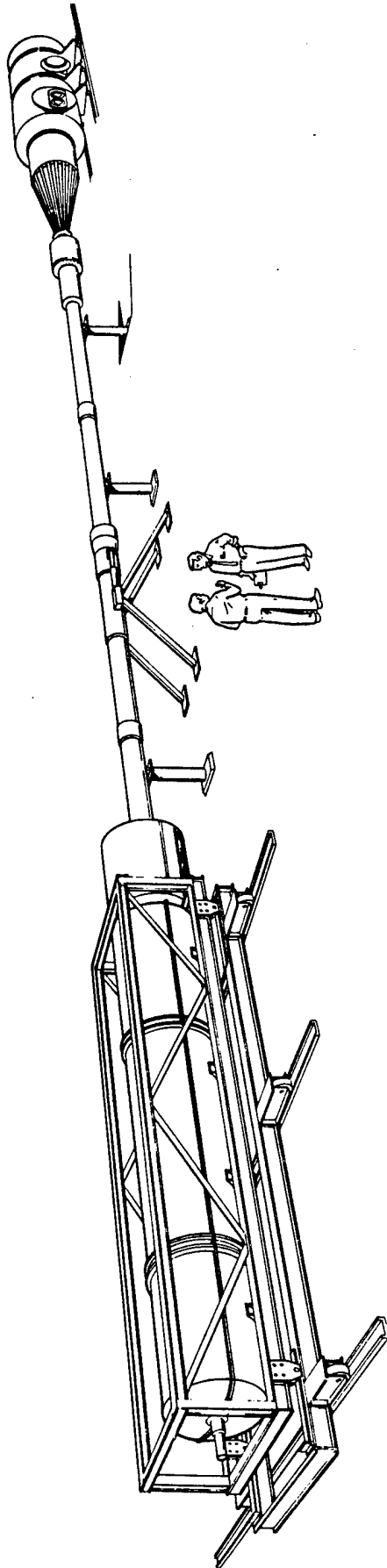


Figure 1 BASIC COMPONENTS OF THE LENS HYPERSONIC SHOCK TUNNEL

## SHOCK TUNNEL OPERATING PRINCIPLES

The shock tunnel is essentially a blow-down facility with a shock compression heater. A shock tunnel is constructed from three major components, the driver tube, the driven tube, and the nozzle and test section. The driven tube is connected to the driver through a fast acting valve called a double-diaphragm rig, which is opened rapidly to start the tunnel. The fast acting centerbody, connected between the driven tube and the nozzle, is used to terminate the flow through the test section to prevent model damage from diaphragm particles. The operation of the 48-inch shock tunnel is shown with the aid of the wave diagram in Figure 2. The tunnel is started by rupturing a double diaphragm that permits high-pressure gas in the driver section to expand into the driven section and, in so doing, to generate a normal shock which propagates through the lower pressure air. A region of high-temperature, high-pressure air is produced between this normal shock front and the gas interface (often referred to as the contact surface) between the driver and driven gas. When the primary or incident shock strikes the end of the driven section, it is reflected, leaving a region of almost stationary, high-pressure, heated air. This air is then expanded through a nozzle to the desired freestream conditions in the test section.

The duration of the flow in the test section is controlled by the interactions between the reflected shock, the interface, and the leading expansion wave generated by the non-stationary expansion process occurring in the driver section. We normally control the initial conditions of the gases in the driver and driven sections so that the gas interface becomes transparent to the reflected shock interaction. This is known as operating under "tailored-interface" conditions. Under these conditions, the test time is controlled by the time taken for the driver/driven interface to reach the throat, or the leading expansion wave to deplete the reservoir of pressure behind the reflected shock; the flow duration is said to be either

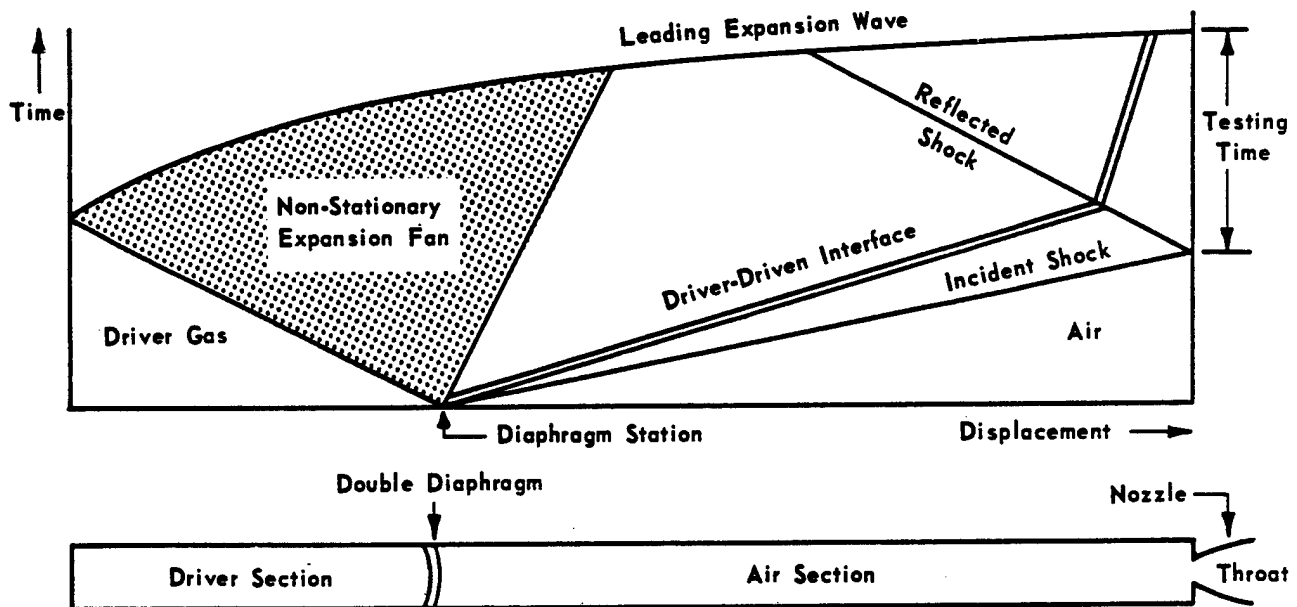


Figure 2 Wave Diagram for Tailored-Interface Shock Tube

driver-gas-limited or expansion-limited, respectively. Low  $Ms_i$  can be used to achieve up to 25 milliseconds test time. When performed under these conditions at high pressures and high Reynolds numbers, the test running times are longer than for piston-driven tunnels with comparable stagnation temperatures, and the reservoir conditions and flow quality are superior to those of piston-driven tunnels. This results from the fact that the test gas is processed by a simple reflected shock rather than by the multiple shocks of piston-driven tunnels. A further consequence is that the freestream conditions can be calculated far more accurately in a shock tunnel.

Note that when sensitive high-frequency instrumentation is used in the very severe heating conditions encountered in interaction regions in hypervelocity flow, running times longer than 20 milliseconds can result in damage to or destruction of the sensing element due to overheating.

## DETAILED OPERATING CHARACTERISTICS

### Flight Corridor

The Hypersonic Shock Tunnel is capable of simultaneously duplicating velocity (i.e., enthalpy) and density over a wide range of hypersonic flight conditions. This range of conditions referenced to a typical continuous flight corridor is shown in Figure 3a for the Calspan 48-inch shock tunnel and the LENS facility. Reservoir temperatures associated with the velocity range of interest are also shown for reference purposes.

Shown in Figure 3b are the reservoir pressures and temperature which must be generated in ground test facilities to duplicate these flight conditions. To generate velocities of up to 14,000 ft/sec at an equivalent altitude of 75,000 requires equilibrium reservoir temperatures approaching 14,000°R and reservoir pressures close to 40,000 psia. While such conditions cannot be generated in facilities with long test times without freestream contamination, they can be produced in short-duration high-energy shock tunnels. It is important to note that for stagnation temperatures above 8,000°R, where real gas effects in air are

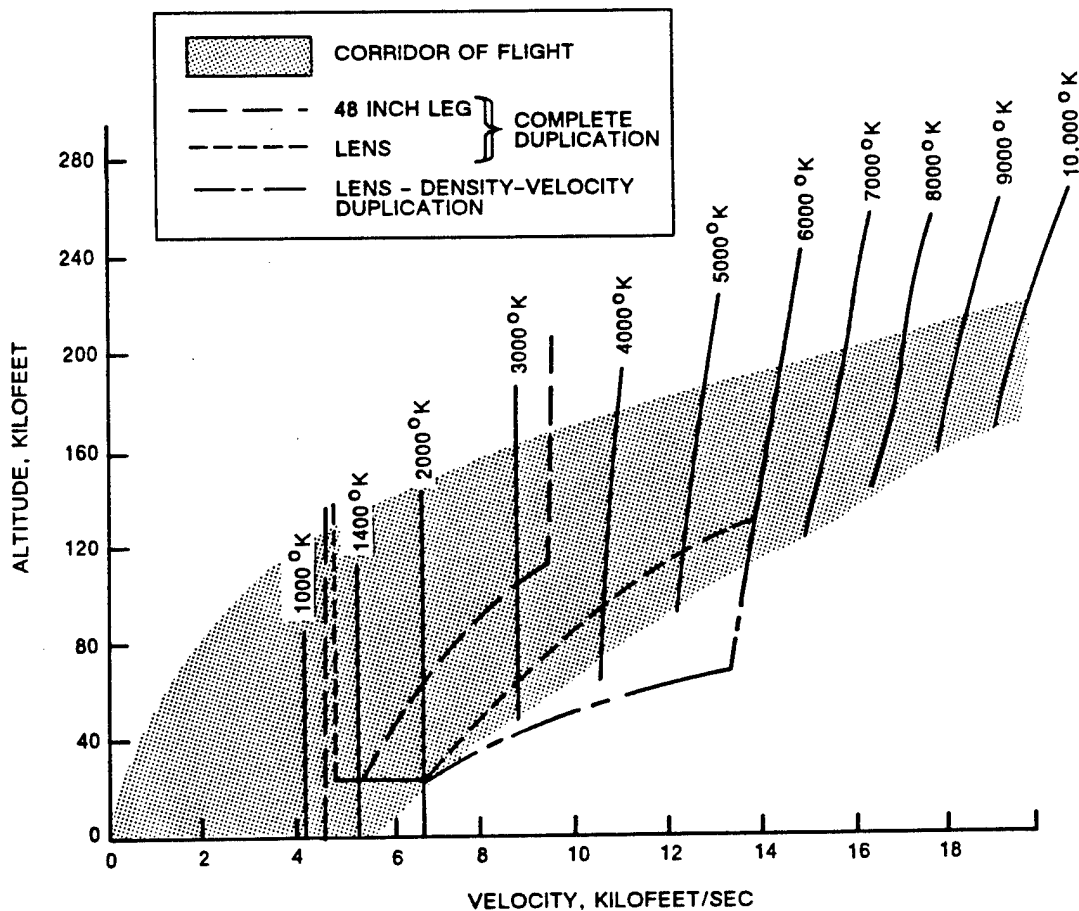


**Figure 3a PERFORMANCE RANGE OF CALSPAN HYPERSONIC SHOCK TUNNEL**

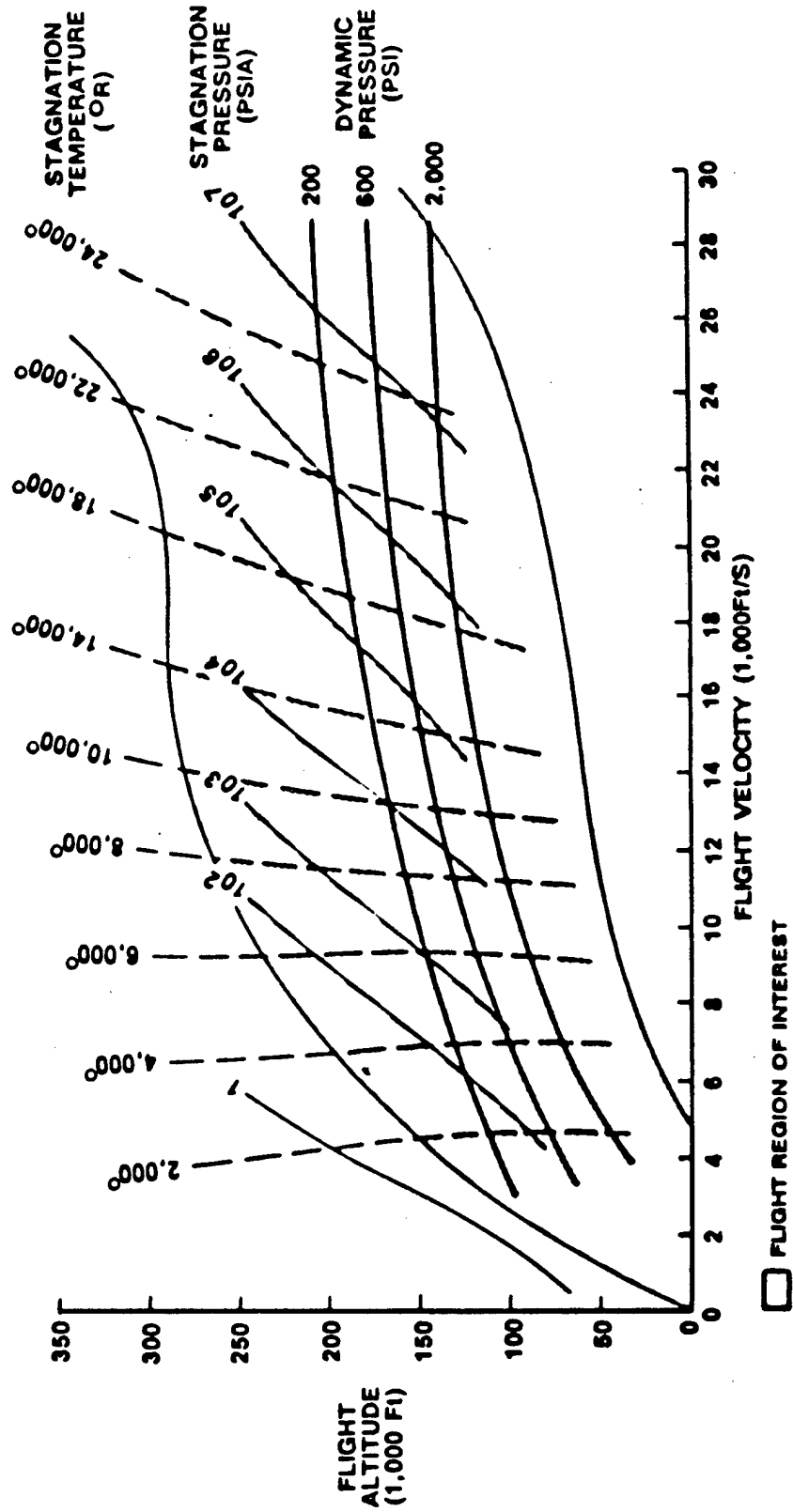


Figure 3b RESERVOIR CONDITIONS FOR GROUND TESTS FLIGHT DUPLICATION

important, reservoir pressures greater than 20,000 psi are required to prevent significant levels of energy being frozen in non-equilibrium species in the gasdynamic expansion to hypersonic freestream conditions.

For certain flow phenomena (e.g., blunt bodies), the important parameters to be duplicated are the density-altitude and the flight velocity. These two parameters then insure duplication of freestream momentum ( $\rho_\infty U_\infty^2$ ) and energy ( $1/2 \rho_\infty U_\infty^3$ ). Duplication of density-altitude and freestream velocity in the shock tunnel implies a higher freestream static temperature than in flight and, hence, a lower Mach number and unit Reynolds number. However, for inviscid flows that are Mach number independent, the lower flow Mach number imposes no restriction provided it is hypersonic (*i.e.*,  $M_\infty \geq 5$ ).

$M_i$  is the primary parameter governing the supply temperature ( $T_o$ ) of the air behind the reflected shock. Figure 4 shows the relationship between  $M_i$ ,  $T_o$  and the total enthalpy  $H_o$ . The effect of supply pressure ( $P_o$ ) of the air behind the reflected shock on  $T_o$  is also shown for 100 and 1,000 atmospheres. In making tunnel performance calculations, it is convenient to use the Mach number ( $M_i$ ) of the shock wave traveling down the shock tube as a reference parameter.

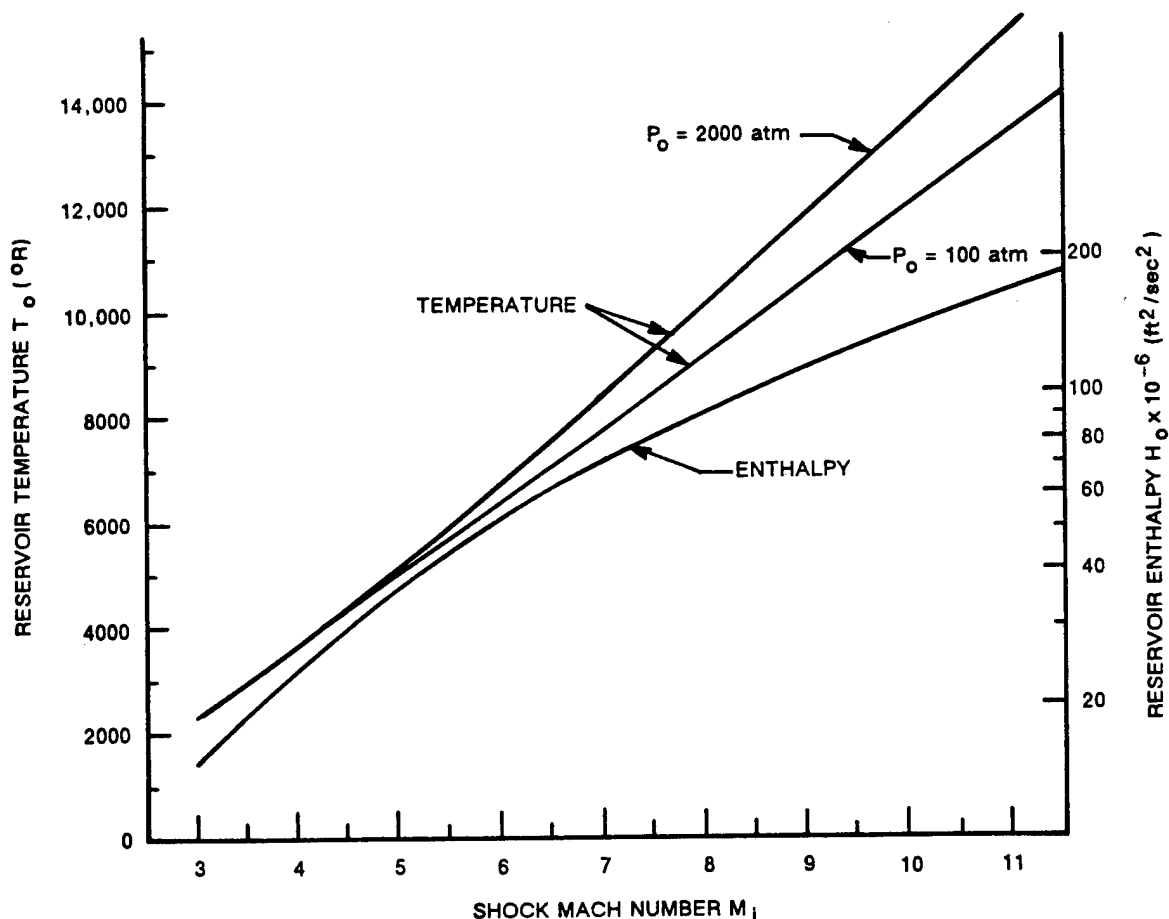


Figure 4 RESERVOIR TEMPERATURE AND ENTHALPY AS A FUNCTION OF SHOCK MACH NUMBER

## Reynolds Number-Mach Number

The performance<sup>4</sup> of the tunnel covers Reynolds numbers (per foot) from  $10^3$  to  $10^8$  and Mach numbers from 5.5 to 24. This Reynolds number-Mach number simulation range is presented in Figure 5. The constant altitude lines shown are those at which a vehicle would have to fly in order to achieve the combinations of Reynolds number per foot and Mach number shown.

It is useful to present the overall capability of the LENS as shown in Figure 6 for representative nozzle air supply pressure levels of 4,000 psia and 30,000 psia. The figure relates the test Mach number, the dynamic pressure, and the freestream Reynolds number to the incident shock Mach number. The highest Reynolds numbers are achieved with the weakest incident shocks (i.e., at the lowest stagnation temperatures). Also shown are the values of  $M_i$  required to duplicate flight enthalpies as are those required to avoid air condensation. The minimum operating temperature is generally taken as that at which oxygen condenses in the test section. Although an increase in unit Reynolds number can be achieved by operating below the condensation limit, (References 2 and 3), past experience has indicated it is necessary to operate at freestream static temperatures approximately 10% above that at which oxygen condensation occurs to insure valid data. This operational philosophy is reflected in Figure 6.

### Test Section Conditions

Test section conditions are calculated under the assumption of isentropic flow from the reservoir to the test section. The test conditions can be computed assuming the test air to be in thermodynamic equilibrium or nonequilibrium.

#### A. Equilibrium

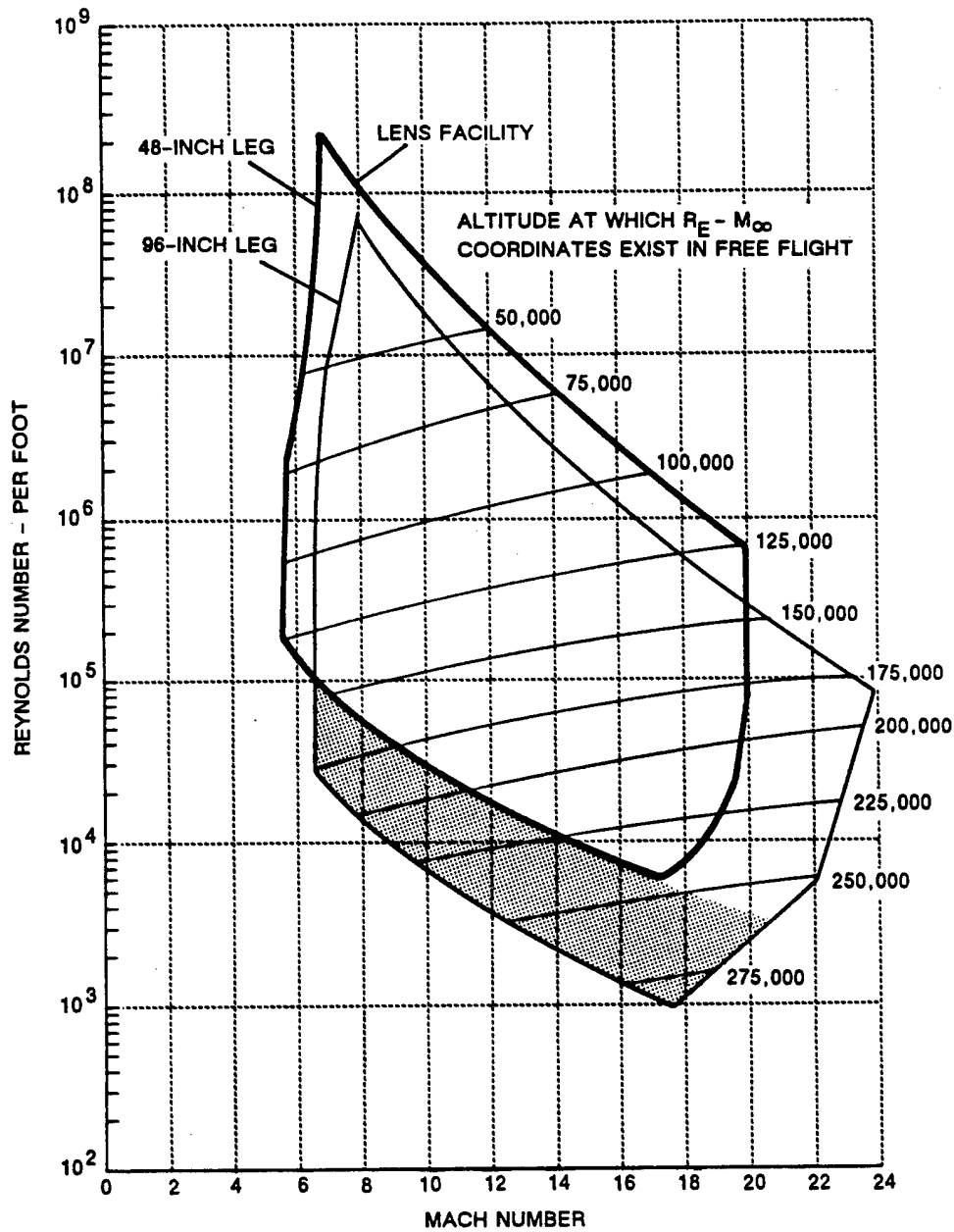
The calculations for test conditions assuming thermodynamic equilibrium in the test section include the vibrational heat capacity of the diatomic oxygen and nitrogen in air.

Test section static temperature is obtained by equating the total enthalpy generated in the shock tube to the stagnation enthalpy in the test section. The test section static temperature is then:

$$T_{\infty} = \frac{h_o}{\bar{C}_{p^{\infty}AVG}} \left[ 1 + \frac{\gamma_{\infty} - 1}{2} \frac{C_{p^{\infty}}}{\bar{C}_{p^{\infty}AVG}} M_{\infty}^2 \right]^{-1}$$

where	$T_{\infty}$	=	test-section static temperature
	$h_o$	=	total enthalpy
	$\bar{R}$	=	specific gas constant
	$M_{\infty}$	=	test section Mach number
	$C_{p^{\infty}AVG}$	=	specific heat at constant pressure
	$\bar{C}_{p^{\infty}AVG}$	=	averaged specific heat at constant pressure
	$\gamma_{\infty}$	=	$\frac{C_{p^{\infty}}/\bar{R}}{(C_{p^{\infty}}/\bar{R} - 1)}$

Now  $C_{p^{\infty}}$  and  $\bar{C}_{p^{\infty}AVG}$  are functions of  $T_{\infty}$ , hence, the calculation of  $T_{\infty}$  for a given  $M_{\infty}$  involves an iterating computation.



$Re_{MAX}$  BASED ON  $T_\infty MIN = 1.10 T_{LOX}$



HIGH  $T_0$ , SHORT TEST TIME REGION ( $t < 2$  ms)  $T_0 > 6000^\circ R$

Figure 5 LENS HYPERSONIC SHOCK TUNNEL PERFORMANCE

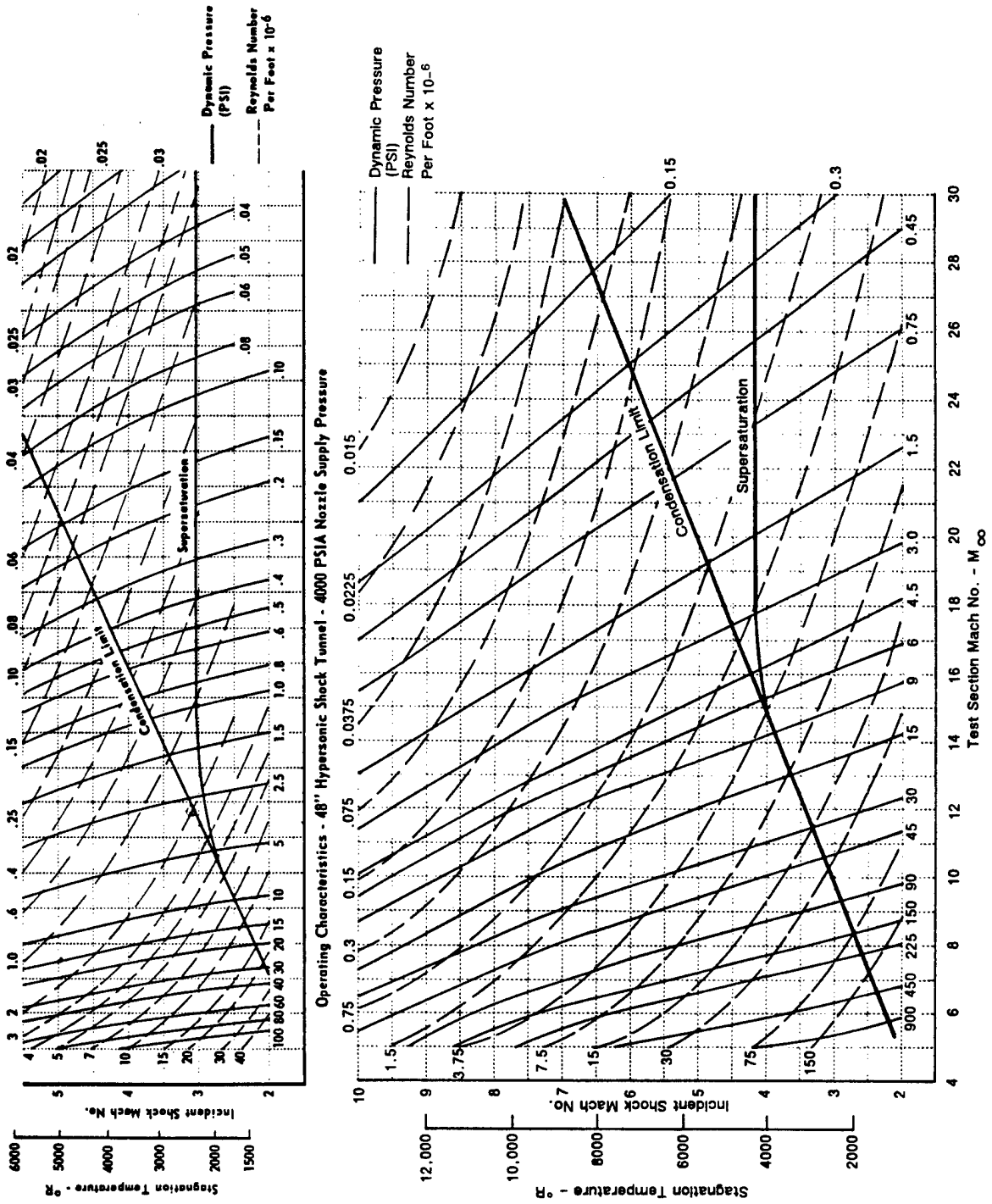


Figure 6 Operating Characteristics - 96" Hypersonic Shock Tunnel - 30,000 psia Nozzle Supply Pressure - Chemical Equilibrium

The test section static pressure is determined as follows:

$$P_{\infty} = P_{ref} \left( \frac{T_{\infty}}{T_{ref}} \right)^{\frac{\gamma}{\gamma-1}} \exp \left( \frac{S_{ref}}{R} - \frac{S_o}{R} \right)$$

where

$S_o$	=	entropy of test air including vibrational contributions
$\frac{S_{ref.}}{R}$	=	30.56
$P_{ref.}$	=	.001 psia
$T_{ref.}$	=	500°R
$\gamma$	=	specific heat ratio for air composed of 20.98% O <sub>2</sub> , 78.08% N <sub>2</sub> , .93%A

The values of  $S_{ref.}$  are obtained from Reference 4 for air at some arbitrary state obeying the perfect gas laws.

The dynamic pressure is:

$$q_{\infty} = \frac{1}{2} \rho_{\infty} u_{\infty}^2$$

where

$$\rho_{\infty} = \frac{p_{\infty}}{RT_{\infty}}, \quad u_{\infty} = \sqrt{\gamma_{\infty} RT_{\infty}} M_{\infty}$$

The test section stagnation pressure is obtained by solving the Rankine-Hugoniot normal shock equation at the test section Mach number and can be shown to be:

$$P'_{o} = p_{\infty} \left[ 1 + \gamma_{\infty} M_{\infty}^2 \left( 1 - \frac{\xi}{2} \right) \right]$$

where  $\xi$  is the ratio of the density ahead of the shock wave to that after the shock.

#### B. Nonequilibrium

For air-supply temperatures above 5800°R, at which some dissociation takes place, care must be taken to include nonequilibrium effects in the nozzle expansion.<sup>5,6</sup> In general, the expansion process is so rapid that finite-rate chemical relaxation processes cannot maintain equilibrium composition, and some residual amounts of dissociated gas species remain when the air reaches the test section. The effects on specific heats, static enthalpy and molecular weight of the residual dissociated gas species and associated frozen chemical energy need to be taken into account in the determination of freestream conditions. For exact computation of these effects, CUBRC has available a computer solution for nozzle expansions with finite-rate chemistry. Solutions for the effects of nonequilibrium in the nozzle expansion on tunnel test

test section condition have been obtained for a wide range of tunnel-supply conditions and nozzle geometries, and new solutions can be obtained for a specific test.

An appropriate solution has been developed which generalizes the computer solutions so that the nonequilibrium effects, including residual (or "frozen") energy in vibration, for a specified test condition can be handcalculated to good accuracy. The frozen atomic specie mole fraction,  $\eta_A$ , and static enthalpy loss through freezing,  $h_f$ , and effect of vibrational freezing on entropy,  $S_{V_F}/R_o$  are found from graphical presentations of the exact solutions. The ratios of nonequilibrium to equilibrium values in the freestream are then:

$$\frac{T_{N.E.}}{T_{EQ}} = \frac{\left[ \left( 1 + \frac{h_f}{2h_o} \right) \left( 1 + \frac{\eta_A}{2} \right) \right]^{2/5(1+\frac{2}{5}\eta_A)} \eta_A^{2/5\eta_A} [f(T_o, P_o)]^{\eta_A} \exp \left( \left( -\frac{2}{5} + \frac{6}{25}\eta_A \right) \frac{S_{V_F}}{R_o} \right)}{\left( \frac{A}{A^*} \right)^{\frac{4\eta_A}{25}}}$$

$$\frac{P_{N.E.}}{P_{EQ}} = \left[ \left( 1 + \frac{h_f}{2h_o} \right) \left( 1 + \frac{\eta_A}{2} \right) \right] \frac{T}{T_{EQ}}$$

$$\left( \frac{M_{N.E.}}{M_{EQ}} \right)^2 = \frac{1 - \frac{h_f}{h_o}}{\left( 1 + \frac{43}{70}\eta_A \right) \frac{T}{T_{EQ}}}$$

where  $T_o, P_o$  = are the reservoir temperature and pressure  
 $h_f/h_o$  = is the fraction of total enthalpy frozen into dissociation and vibrational excitation  
 $\eta_A$  = is the mole fraction of atomic species  
 $A/A^*$  = is the local area ratio  
 $S_{V_F}/R_o$  = is the non-dimensional entropy of the gas at the temperature of vibrational freezing

N.E. and EQ as subscripts refer to nonequilibrium and equilibrium conditions, respectively

This approximate analysis has also been applied to aerodynamic shapes to determine those conditions for which knowledge of freestream nonequilibrium is important; these results assist in the assessment of the degree of accuracy to which the nonequilibrium effects must be determined for a given test.

### Testing Time

The duration of steady airflow is limited in the tailored case by the downstream propagation of expansion waves from the driver section, which upon arrival at the downstream end of the driven tube, decrease the pressure and temperature of the nozzle supply gas. A second factor, which limits the available test time at higher incident shock speeds, is the penetration of the interface by the driver gas and the resulting

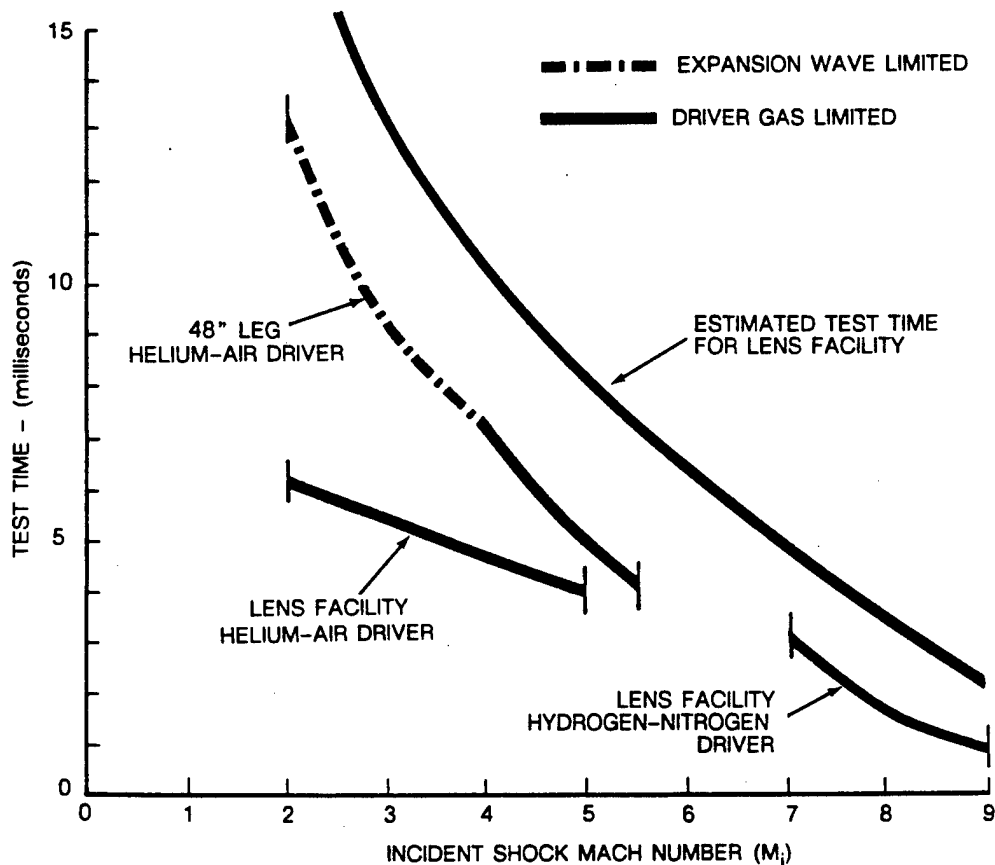


**Figure 7 TEST TIME AVAILABLE FOR TAILORED INTERFACE OPERATION**

early arrival of driver gas in the test section. This phenomena has been studied both experimentally and theoretically, and test time limitations based upon it are well known.<sup>15</sup> The testing time for various operating conditions are shown in Figure 7. Additional test time can be attained in the 48-inch Leg at incident shock speeds below 3.5 by increasing the driver length to 40-feet.

#### **Observations on Boundary Layer Transition in Hypersonic Flows**

Experimental measurements of boundary transition on sharp flat plates and cones made in many different studies conducted in the Calspan 48- and 96-inch shock tunnels, which have the same nozzle configurations as the LENS facility, form the basis for the correlations presented herein. We have also selected measurements and observations from ballistic range and downrange shots for comparison. It is clear from the studies of Pate and Schueler<sup>37</sup> and extensive measurements made at NASA Langley that boundary layer transition on models in wind tunnel studies is influenced by the freestream pressure environment. In general, our studies were conducted at Mach and Reynolds numbers considerably larger than those in the studies of Pate and Schueler. Thus, the magnitude of the noise radiated from the tunnel walls and the intensity on the axis should be significantly less in these facilities. A direct result of Pate and Schueler's findings is that a decrease in the tunnel size, for the same freestream conditions, should decrease the transition Reynolds number. However, transition measurements (shown in Figure 8a) made in the A and D nozzles, which have exit diameters of 24 and 48-inches, respectively, do not exhibit this

scale effect, even though a unit Reynolds number variation is evident in the correlation. Predictions based on Pate and Schueler's correlation suggest transition Reynolds numbers of over 200 million should be anticipated for our test conditions, which is clearly well in excess of physically meaningful values. Expressing transition in terms of the Reynolds number based on the momentum thickness at transition onset, we can compare our measurements with the results of earlier studies conducted in the ballistic range and on full scale flight tests as shown in Figure 8b. Here we have included measurements from cone and flat plate studies; we can see that, although our transition measurements on flat plates are consistently larger than those on cones, both sets of measurements are in essential agreement with ballistic range and flight tests. It is clear that in these tests the position of transition was influenced by factors more complex than those governing transition in the tests conducted by Pate and Schueler. Whether the fluctuating pressure level of the freestream is the principal factor influencing transition, as indicated by the measurements of Stainback, Fisher, and Wagner,<sup>38</sup> or whether this quantity is directly related to parameters which themselves govern transition remains to be determined.

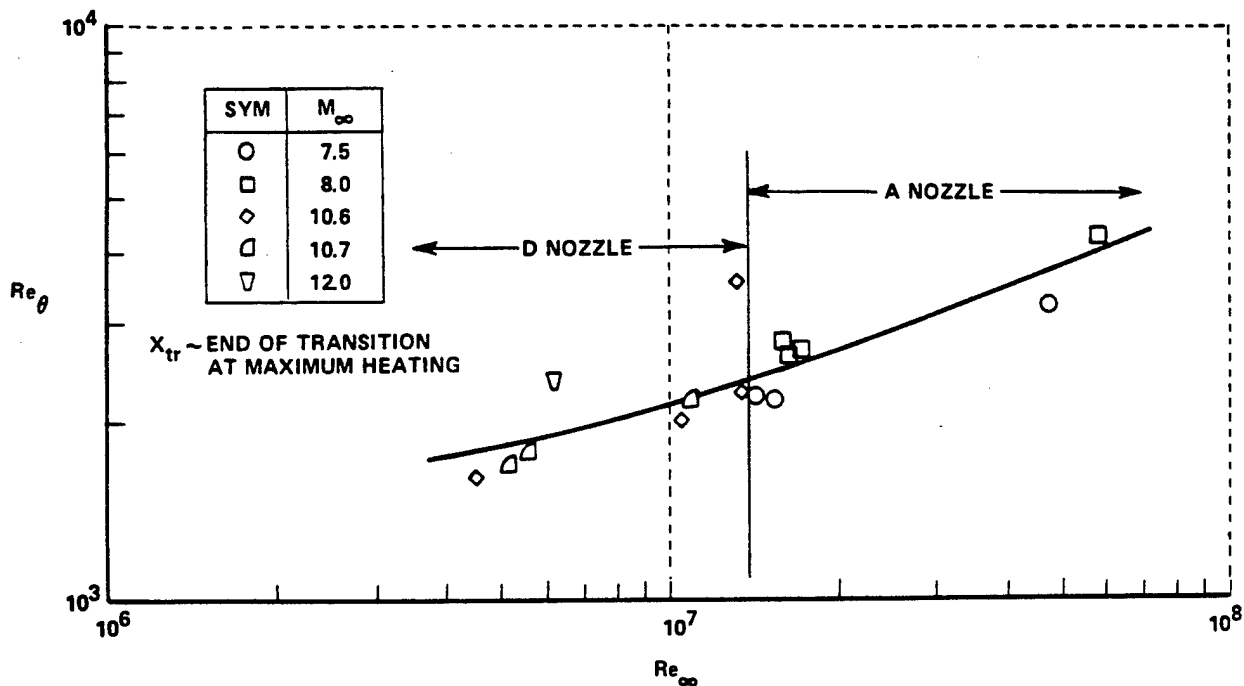
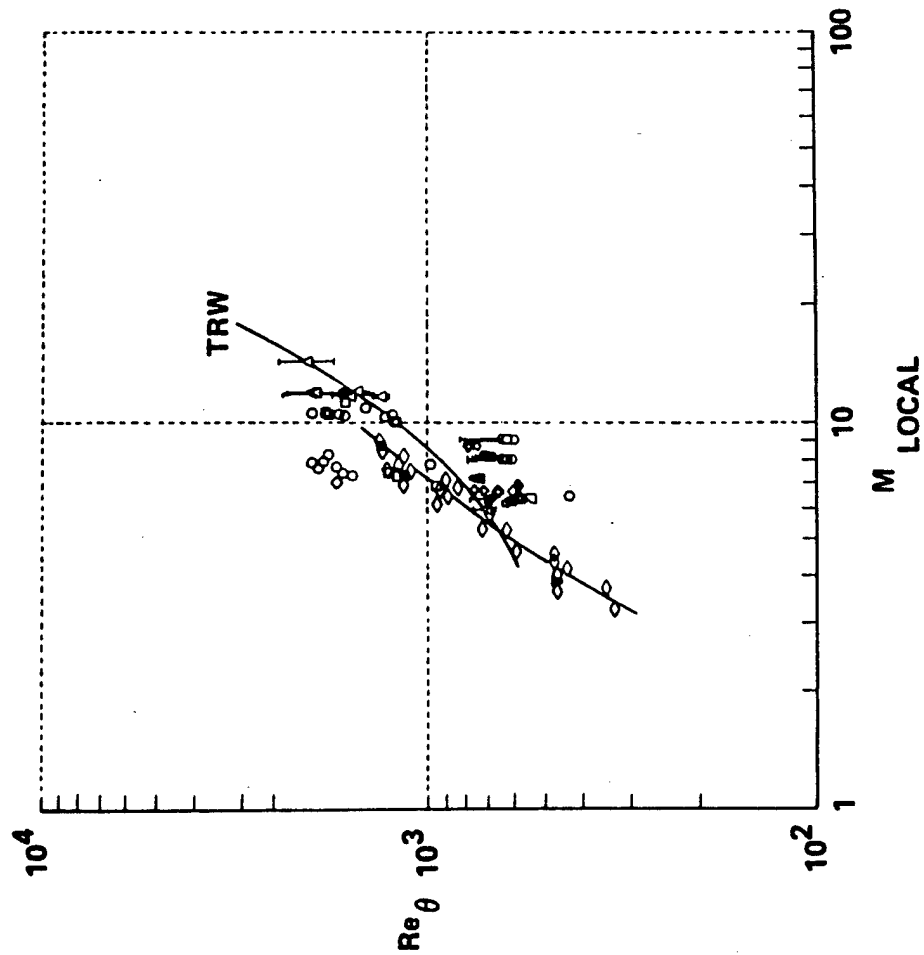


Figure 8a CORRELATION OF TRANSITION SHOWING THE EFFECTS OF TUNNEL SIZE



SYM	MODEL	SOURCE
○ □	F.P. ↓	260 + K90 RTD C86W <sub>7</sub> N <sub>1</sub>
◇ △ ○ ◊	CONES 6.5° 6°20' 8.5° 9° 7.5° 6.5° 5°	LKHD CC H49 MDAC G86 MDAC RVTO LKHD H28   LKHD H40 ↓
△ ◇	3°-9°	TRW FLIGHT BALLISTIC RANGE

Figure 8b CORRELATION OF TRANSITION MEASUREMENTS IN THE CALSPAN SHOCK TUNNELS WITH BALLISTIC AND DOWNRANGE MEASUREMENTS

## NON-CONVENTIONAL TESTING

Non-conventional test programs have included: hydrogen fuel injection, mixing, and combustion tests of supersonic combustor models; external burning and fuel rich jet interaction studies in a hypersonic stream with hydrogen, pyrophoric fuels, bipropellants, and solid propellants; transpiration cooling,<sup>13</sup> studies of boundary layer<sup>14,27,28,29</sup> and wake phenomena,<sup>10,31</sup> mass addition, nuclear-hydrogen rocket throat heating; the use of a double shock tube to develop a blast wave in a hypersonic stream;<sup>11</sup> microwave-plasma interaction experiments; refraction and dispersion of light by shock waves and turbulent flow. Figure 9a shows a typical comparison of SCRAMJET combustor data obtained from the shock tunnel to the latest code prediction.

### Microwave Propagation Research Capability

At high shock speeds, the ionized flow conditions generated about test models allow tests designed to investigate the interactions of microwaves with such plasmas (Figure 9b). Electron densities in the order of  $10^{14}/\text{cc}$  are obtained in the strong shock region about blunt bodies and up to  $10^{11}/\text{cc}$  in wakes. Programs which have been conducted include microwave and VHF transmission to and from plasma sheathed vehicles<sup>7</sup>, antenna breakdown studies<sup>8</sup>, magnetic field interaction studies<sup>9</sup>, wake cross section investigations and electron probe instrumentation development<sup>10</sup>. Available for this type of test is a microwave test section designed specifically for transmission of electromagnetic waves<sup>11</sup>. It is 4-feet in diameter and 10-feet long and is made of 10 layers of Fiberglas honeycomb sandwiched between eleven layers of mylar. Its reflection coefficient is less than 20 dB over a range of frequencies from VHF through X-band. It is compatible with the pressures and loads developed by shock tunnel testing. An X-band interferometer is available for monitoring both nozzle flow electron density and wake probing. A short pulse doppler radar<sup>12</sup> can also be made available for special studies of model or wake cross section as well as detailed probing of wakes. The electron beam and miniature pitot and heat transfer probe rakes as well as electrostatic probes are available for point probing of the model flowfield and wake<sup>10</sup>.

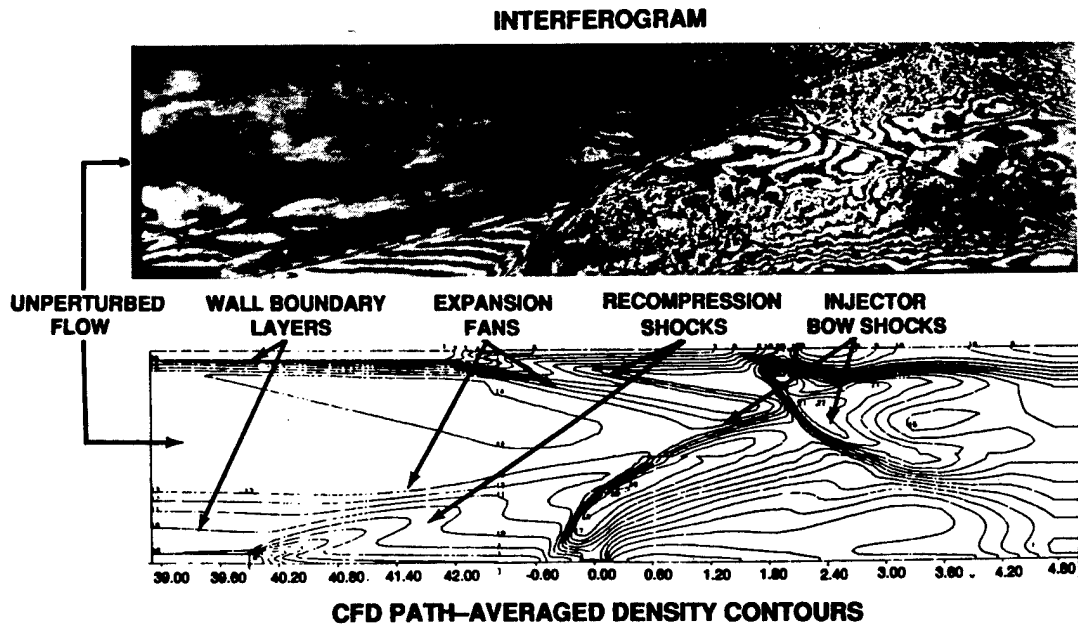


Figure 9a INTERFEROGRAM-CFD PATH-AVERAGED DENSITY CONTOUR COMPARISON

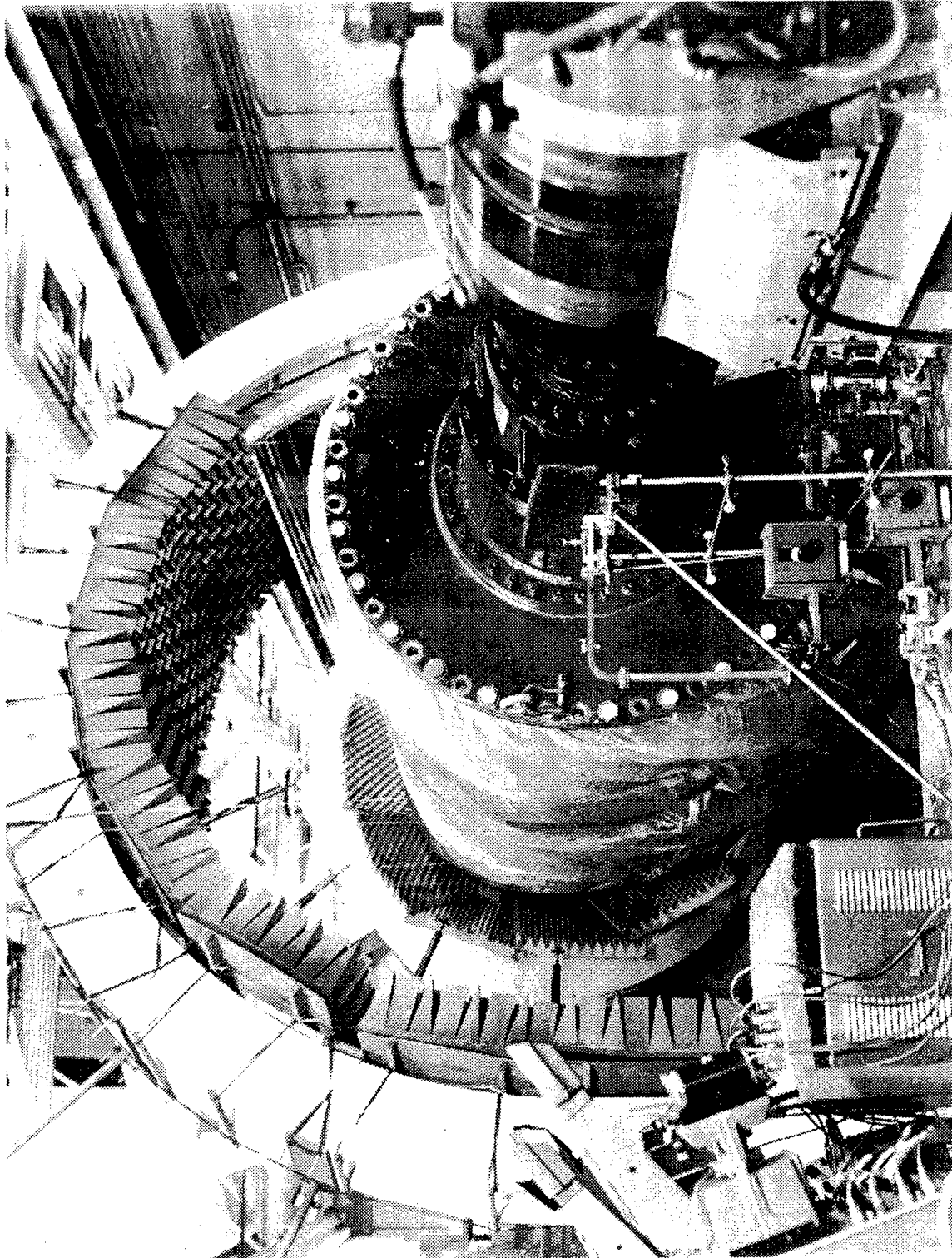


Figure 9b TUNNEL CONFIGURATION FOR EXPERIMENTAL INVESTIGATION OF MICROWAVE PLASMA INTERACTION STUDY

## GENERAL AIRFLOW DATA AND CALIBRATION

The test conditions generated by each nozzle are functions of several variables: nozzle throat size, air supply pressure and temperature, and in the case of a conical nozzle, axial station in the test section. The lateral distribution of pitot pressure has been surveyed in each nozzle for many combinations of these variables; examples are shown in the lower left-hand corners of Figures 10 and 11.

Airflow data from many runs of a particular nozzle configuration are averaged for each run and the average values are normalized to standard conditions as shown in Figures 10 and 11 to indicate their dependence on supply conditions. The theoretical trends are established based upon the best available boundary layer information<sup>14</sup>. It has been found that data taken in the 96-inch leg duplicates that obtained in the 48-inch leg. Therefore, the  $M_\infty$  vs.  $M_i$  curves are applicable to both legs of the tunnel within their respective limits, and the LENS shock tunnel

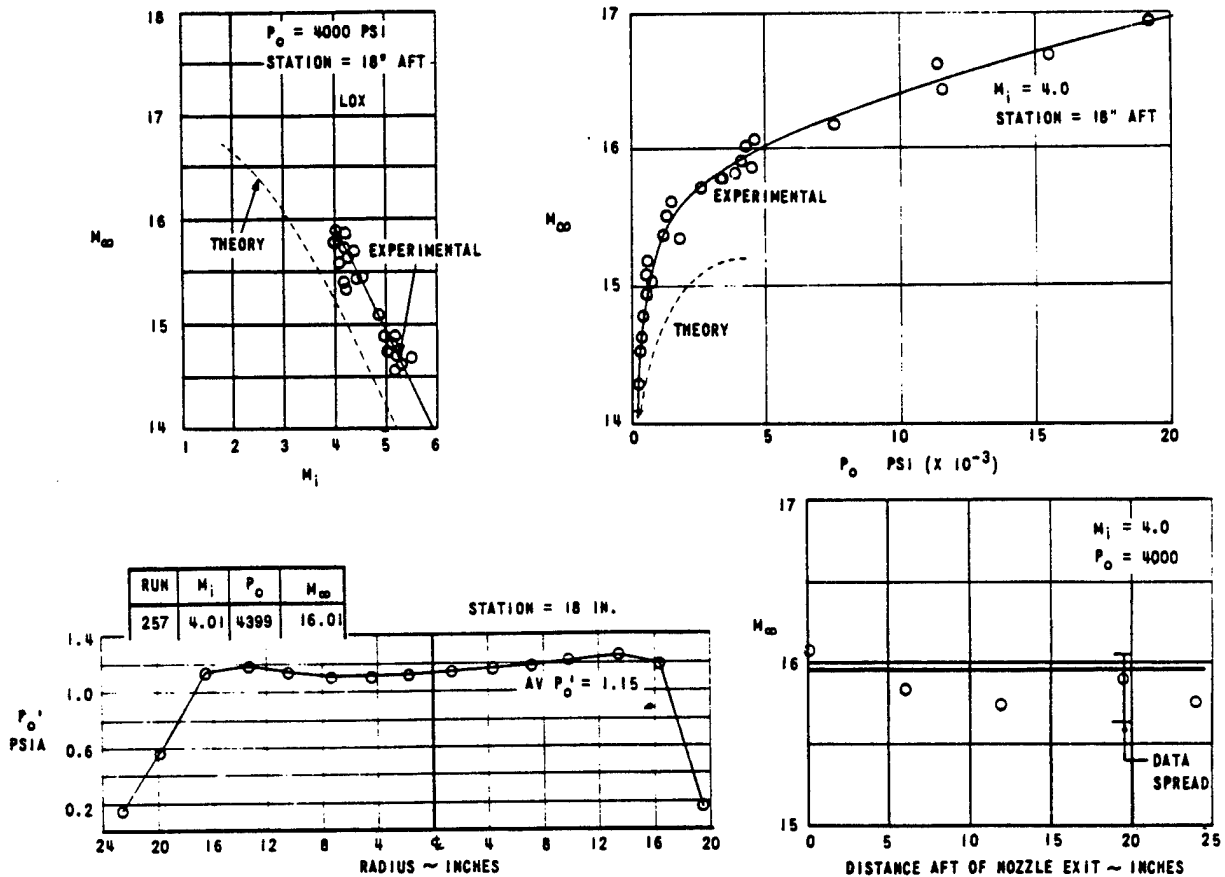


Figure 10 AIRFLOW CALIBRATION - 4-FOOT CONTOURED "D" NOZZLE  $D^* = 0.5$ -INCHES

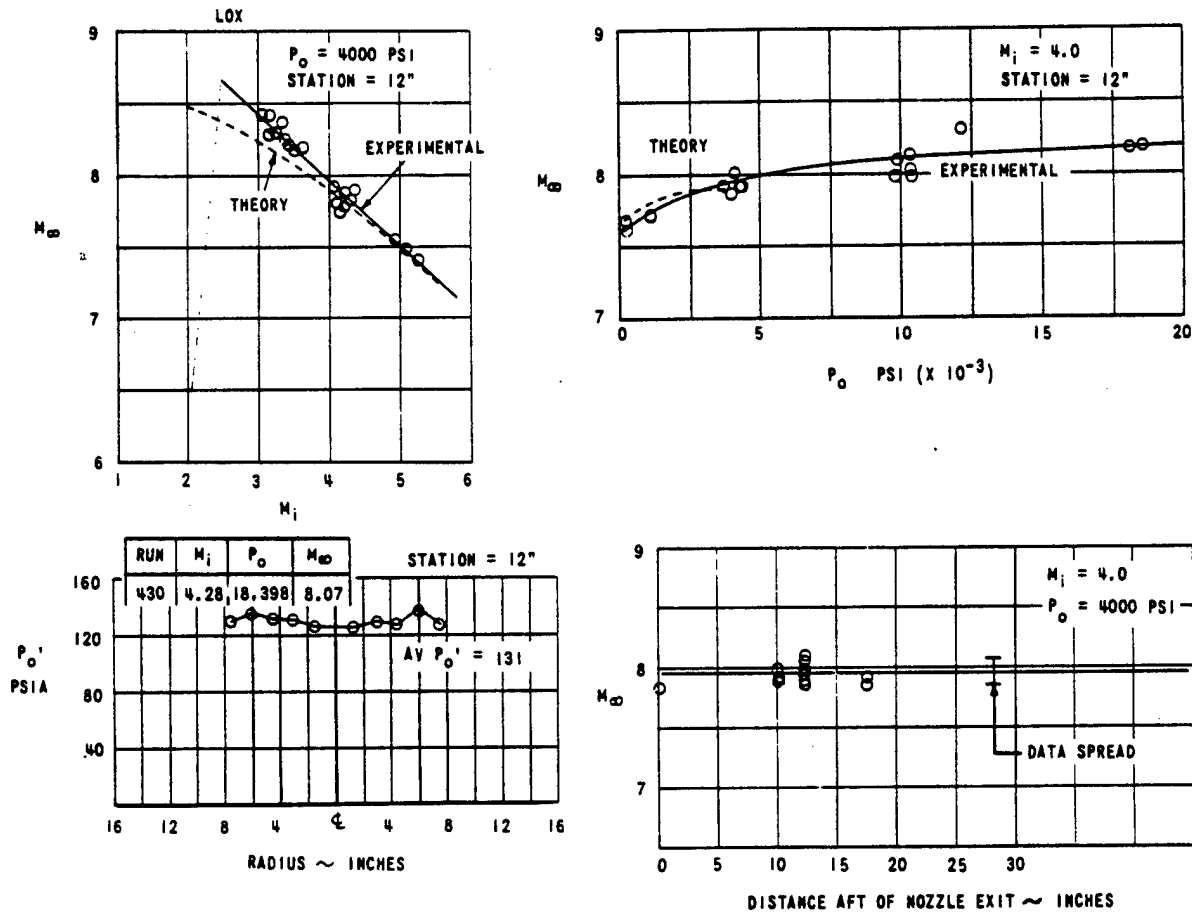


Figure 11 AIRFLOW CALIBRATION - 2-FOOT CONTOURED "A" NOZZLE  $D^* = 1.363$ -INCHES

## INSTRUMENTATION

The 3- to 18-millisecond test time available from tailored-interface operation permits accurate measurement of model pressures, forces, heat transfer rates, and skin friction, as well as flowfield measurements of pitot pressure, total temperature. Additional instrumentation developments include direct gas-sampling probes and instrumentation associated with microwave transmission through the plasma sheath<sup>7</sup>, electron beam density measurements, transpiration cooling<sup>13</sup>, behavior of molten metal droplets in an oxidizing hypersonic airstream<sup>16</sup>, refraction and dispersion effects of the shock wave and turbulent airstream on a culminated beam of light, and the simulation of nuclear blast on a reentry vehicle<sup>11</sup>.

### Pressure

Our piezo-electric pressure transducers<sup>17,18</sup> employ quartz and lead zirconium titanate piezo-electric ceramics as pressure sensitive energy sources and field effects transistors (FET) as power amplifiers<sup>19</sup>. The complete transducers, including the FET, are typically 0.37-inch in diameter and 0.23-inch thick, making them ideally suited for model and pressure rake installations. Transducers of several different types are available with a combined pressure range of from 0.0005 psia to several hundred psia. To provide acceleration compensation, an additional diaphragm-ceramic unit wired in opposition to the active unit is incorporated; this design reduces acceleration sensitivity to a measured value as low as 0.0001 psi/g. A heat shield minimizes temperature and radiation effects. We also use Kulite 0.062-inch diameter solid-state strain transducers. While the dynamic range of these transducers are significantly less than the piezo-electric transducers their small size of makes them valuable for probe instrumentation and where high spatial resolution and high frequency response is required.

A typical transducer, its calibration, and a typical shock-tunnel pitot pressure record are shown in Figure 12; installation of the pressure transducer rake on a model is shown by Figure 13. The transducer has a precision of 1%; the overall accuracy of the pressure measurement in the shock tunnel is 5%.

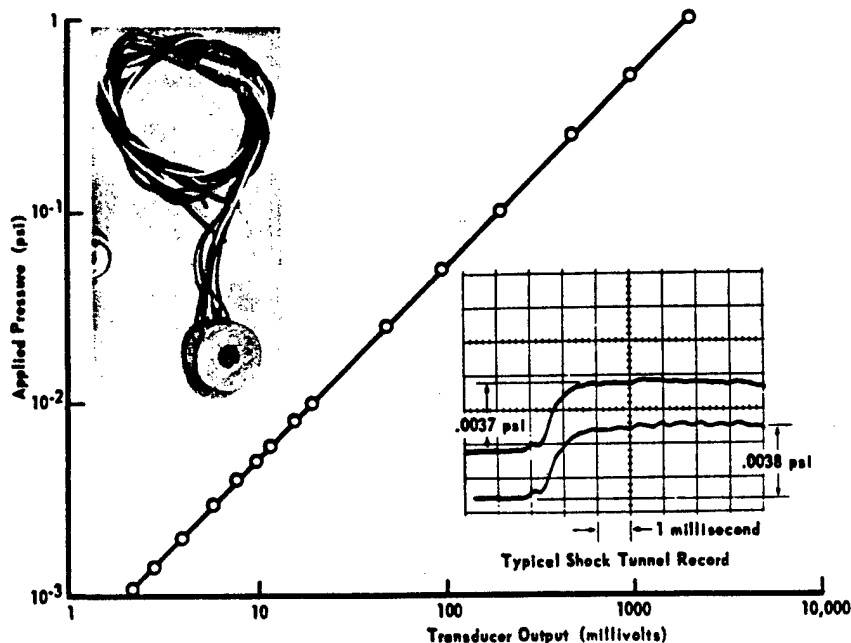


Figure 12 Calspan Piezo-Electric Pressure Transducer

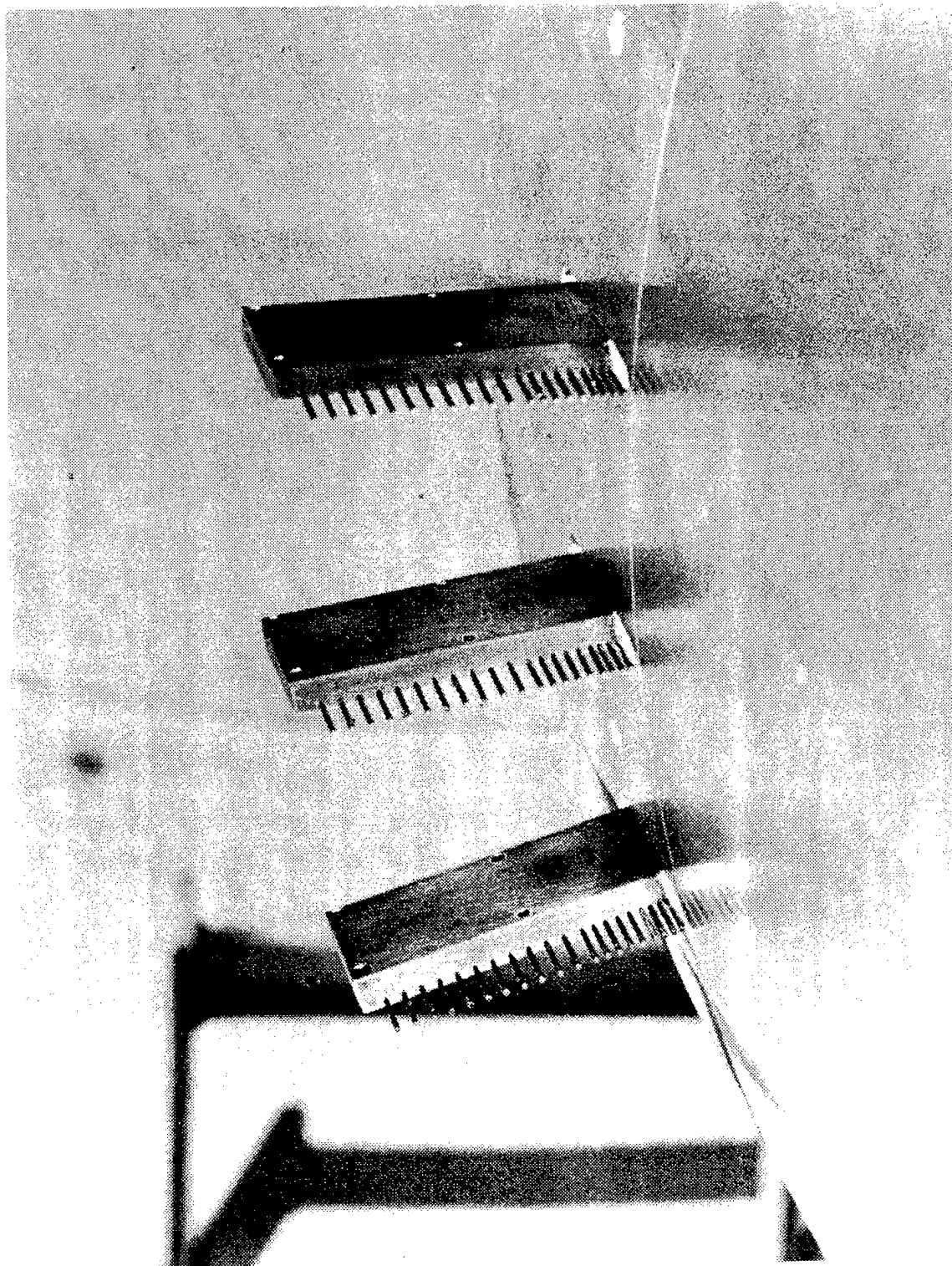


Figure 13 MODEL ASSEMBLY OF PITOT PRESSURE AND TEMPERATURE RAKES

The transducers<sup>20</sup> are calibrated after installation in the model. The voltage variation is linear over the range of pressure normally encountered during testing. These calibrations, in conjunction with estimated values for model pressures to be experienced during the actual test, also provide the basis for adjusting the gains in the data recording system to achieve maximum readability.

In addition to the surface mounted instrumentations discussed earlier, special purpose boundary layer pitot pressure rakes have been developed (Figure 14a). This instrumentation consists of rake-mounted high frequency response kulite pressure transducers. A typical pitot pressure gages have .001-inch diameter orifices and are staggered to .03-inch resolution near wall and .06-inch resolution in the outer wake regions. These small gages (Figure 14b) also enable measurements of pressure fluctuations associated with turbulent boundary layers up to 150 KHZ. The uncertainty of the mean measurements can be shown to be  $\pm 3\%$ .

### Heat Transfer

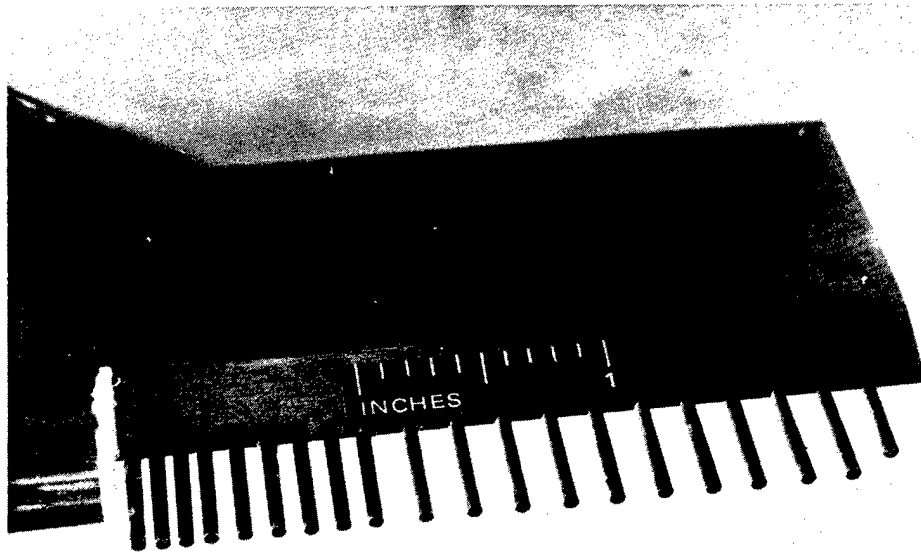
The measurement of heat transfer rates relies on sensing the transient surface temperature of the model by means of thin-film resistance thermometers<sup>18,21,22</sup>. These gages are fabricated either on small pyrex buttons or on contoured strips of pyrex. A typical gage consists of a thin film of platinum, approximately 0.1 micron thick by 5 mm by 0.5 mm, fused to a pyrex model insert.

To insulate the metallic film from the ionized gas stream, a thin dielectric coating of magnesium fluoride is deposited on the surface of the gage. As the heat capacity of the gage is negligible, the film temperature is a measure of the instantaneous surface temperature of the pyrex and is related to the heat transfer rate by the classical equation of heat transfer into a semi-infinite slab of known thermal characteristics. Analysis has shown this technique to be valid for 0.1-micron-thick gages during the short duration of a shock-tunnel test.

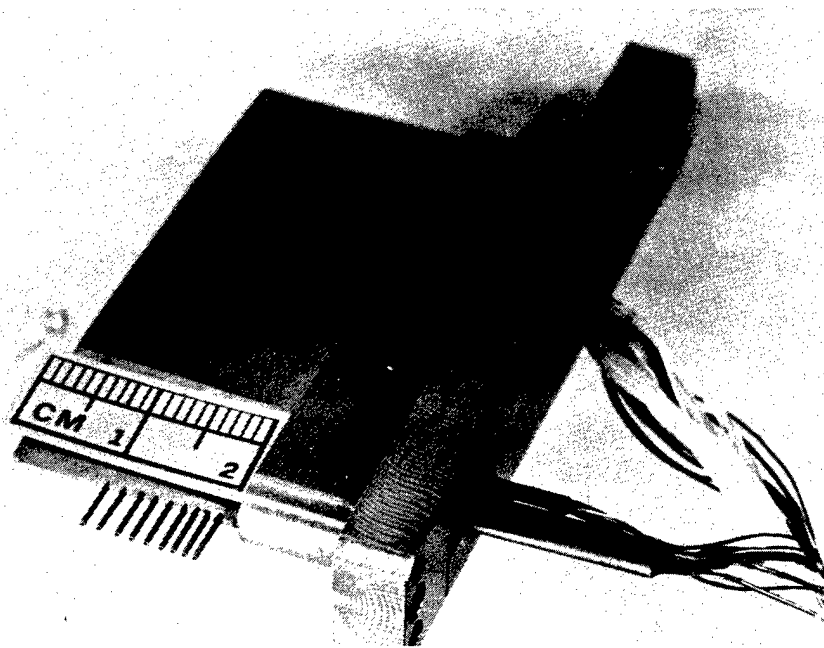
Two characteristics inherent in the thin-film technique make this approach highly successful in obtaining accurate quantitative heat transfer rate data in regions with high thermal gradients such as small radius leading or sharp edges, cavities and surfaces with boundary layer shock wave interactions. First, the low thermal conductivity of the pyrex substrate minimizes lateral conduction and eliminates distortion of high thermal gradients. Secondly, the films can be applied at close intervals which allows high spatial resolution. This technique is used to build the SILTS pod/vertical tail of a .0175 scale space shuttle model<sup>36</sup> as shown in Figure 15a. The SILTS pod/vertical tail was instrumented with 92 thin-film resistance thermometer gages. The upper 30% span of the vertical tail was instrumented with 42 gages on the dome and 9 gages on the left side of the pod fairing to the vertical tail as illustrated by Figure 15b. A typical comparison of the shock tunnel heat transfer data to the shuttle flight data (STS-1, 2, 3) is shown in Figure 15c.

We also designed and developed total temperature gages with 1 millisecond response time. The total temperature gages were designed to be small enough to resolve the total temperature in the wall layer and rugged enough to be able to withstand large variations of static and dynamic pressure generated by hypersonic flows. A typical total temperature probe is 0.03-inches in diameter and uses a 0.0003-inch platinum rodium thermocouple in an arrangement schematically shown in Figure 16a. Figure 16b shows a typical total temperature rake arrangement.

Rae-Taulbee algorithm,<sup>35</sup> which accounts for variable thermal properties, is used to compute the heat transfer rates from the measured by the heat transfer gages.



(a)



(b)

Figure 14 PITOT PRESSURE RAKE WITH KULITE PRESSURE TRANSDUCERS

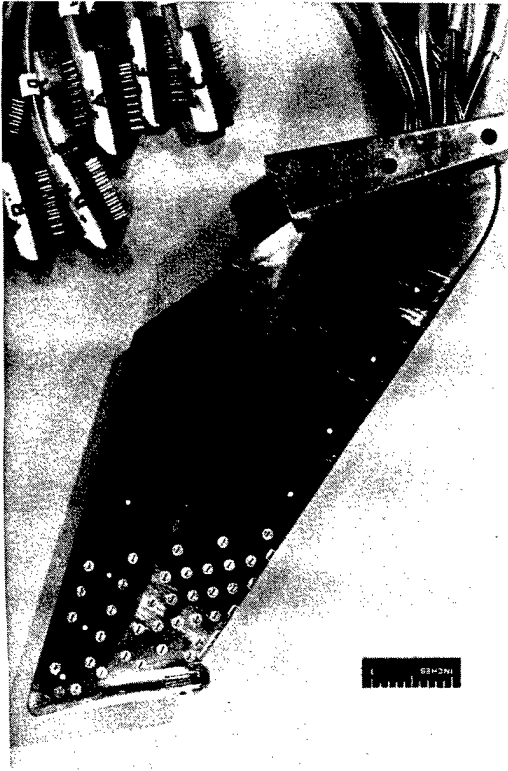


Figure 15a 0.0175-SCALE VERTICAL TAIL WITH SILTS POD

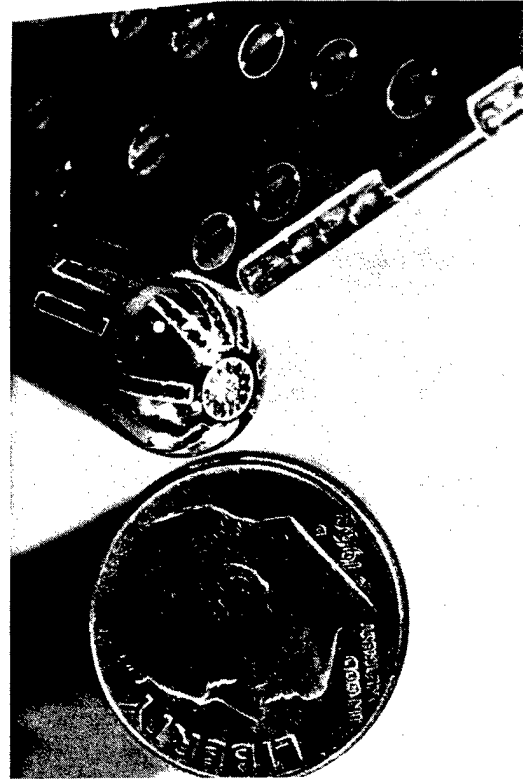


Figure 15b CLOSEUP OF THE SILTS POD

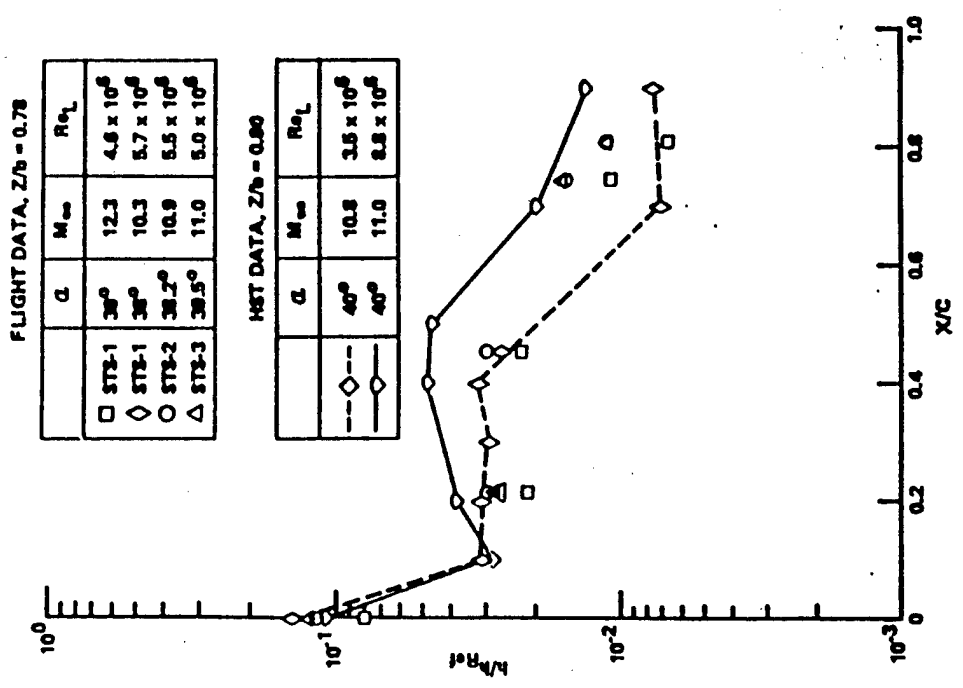


Figure 15c COMPARISON OF FLIGHT AND SHOCK TUNNEL HEAT TRANSFER DATA ON SIDE OF ORBITER VERTICAL TAIL,  $M_\infty = 11$

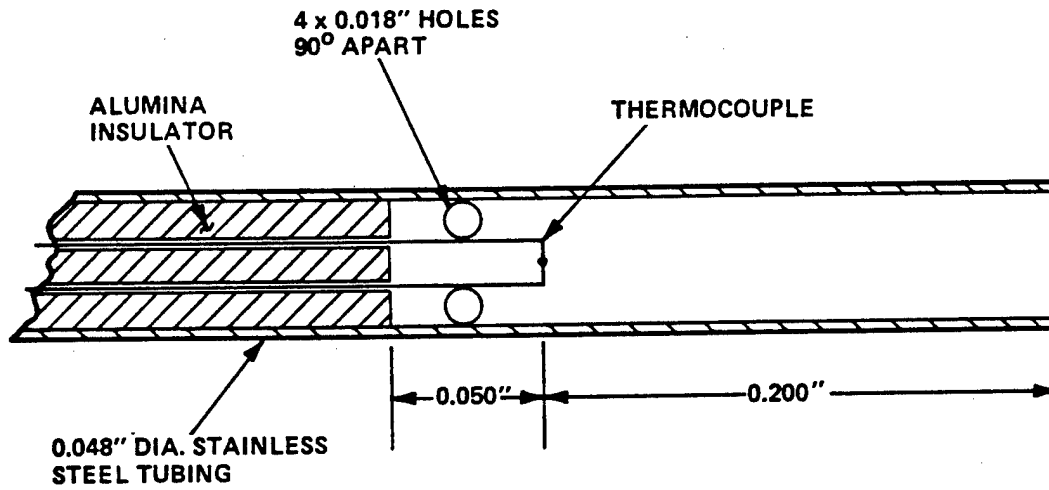


Figure 16a SCHEMATIC DIAGRAM OF TOTAL TEMPERATURE GAGE



Figure 16b TOTAL TEMPERATURE RAKE

The heat-transfer gages are calibrated prior to tests to determine the change in resistance of the elements with temperature. These calibrations are then used to set the recording equipment for the expected temperature increases.

### Thermal Mapping

Isothermal contours (thermal maps) which allow an assessment of heat transfer rate distribution on a spatially continuous basis may be obtained on models in the shock tunnel through the use of rapid response thermographic phosphors<sup>23</sup>. (Thermographic phosphors are those which emit light under the influence of an exciting agent, the brightness being temperature sensitive). In this application the phosphor, painted over a model surface of low thermal conductivity, is illuminated with ultraviolet light. The phosphor fluoresces with a brightness which is inversely proportional to its temperature. Temperature variations of the order of 1°C can be detected. As the model temperature increases during a run the phosphorescence is partially quenched; at some time during the run a black and white photograph of the model is taken which records the brightness distribution over the entire view of the model in terms of film density. If that recorded brightness is subtracted from the ambient temperature wind off brightness, the temperature rise can be determined and the heat transfer rate calculated from semi-infinite slab theory.

In practice the subtraction of wind off brightness is accomplished photometrically and the resultant photograph transformed into isodensity bands (i.e., isothermal bands) with an isodensitracer. A Data Color System, which is essentially an isodensitracer that displays the isodensity bands in the form of discrete colors on a television screen is used in our system. This display is photographed with color film to obtain a permanent record and the colors are correlated with a few thin film gages also placed on the model. This correlation technique avoids the necessity of an absolute calibration of the temperature brightness sensitivity. A black and white photograph of the fluorescence pattern produced by a swept shock-boundary layer interaction in an axial corner is shown in Figure 17. The dark areas are those of relatively higher heating.

The paint is thermally reversible and may be used on succeeding runs without further model preparation.

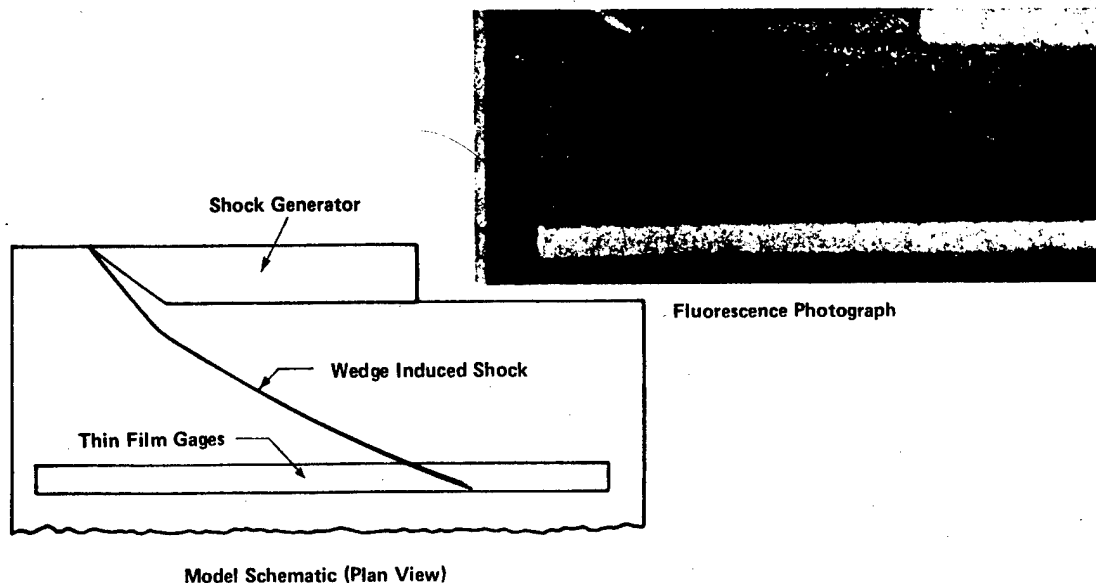


Figure 17 Fluorescence Pattern Produced by Swept Shock-Boundary Layer Interaction

## Force and Moment Measurement

The hypersonic shock tunnel starting process produces a reasonably pure step force on the model which is resisted by the force-measuring capsule and the model inertia. The system then vibrates at its natural frequency determined by the balance spring constant and model mass; other frequencies are also present.

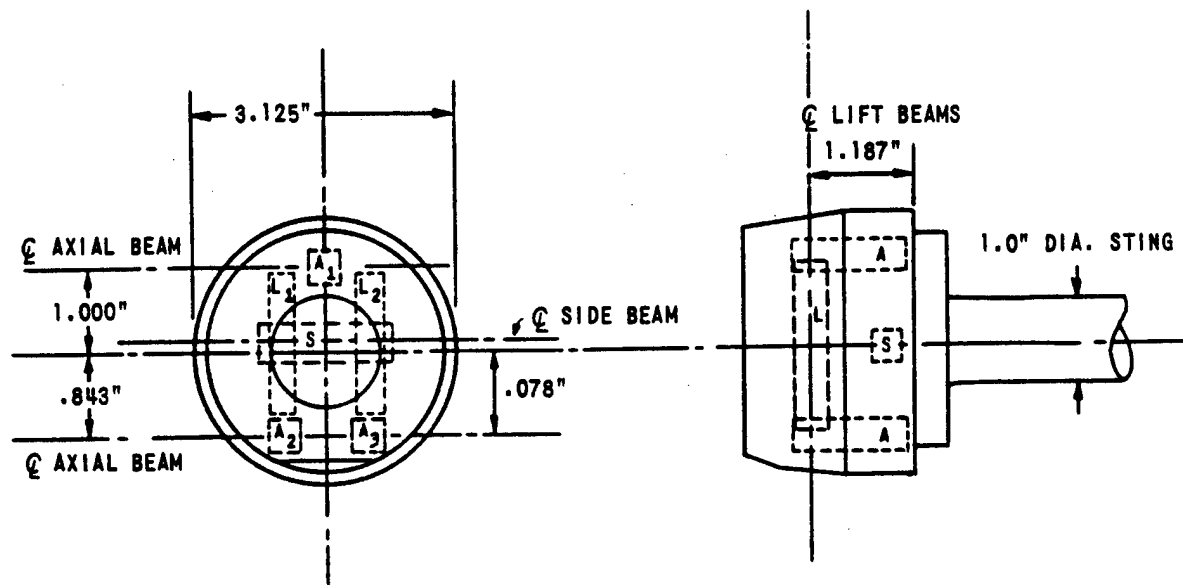
The force balance<sup>17,18</sup> is a more or less conventional internal balance. Acceleration compensation is provided by several accelerometers (equal to the number of force components) mounted internally in the model. By adding to the balance force signal a signal proportional to the model acceleration, the true representation of the airload may be recovered. By the use of light materials (such as magnesium) in the model, it is possible to produce a useful accelerometer signal. The balances which have been built are force-type balances, although moment-measuring balances could also be acceleration compensated; the force-type balance allows lighter models to be used.

Piezoelectric materials are generally used as sensing elements in the force capsules allowing the design of stiff, compact balances having wide dynamic ranges. For instance, a force capsule with an allowable capacity of 100 pounds is capable of measuring a force as small as .01 pound. The miniature accelerometers which have been designed for installation in force models also employ piezoelectric materials.

Several balances are available which are adaptable to a wide variety of model shapes and loads. The characteristics of the F, H and M balances are presented in the table below. Schematic diagrams of the F and H balances are shown in Figure 18. A photograph of the H balance is shown in Figure 19 along with an exploded view of a single force capsule. The M balance utilizes strain gaged beams and was specifically built for use with slender lifting body configurations being tested at high Reynolds numbers, such as can be obtained in the Calspan hypersonic shock tunnel.

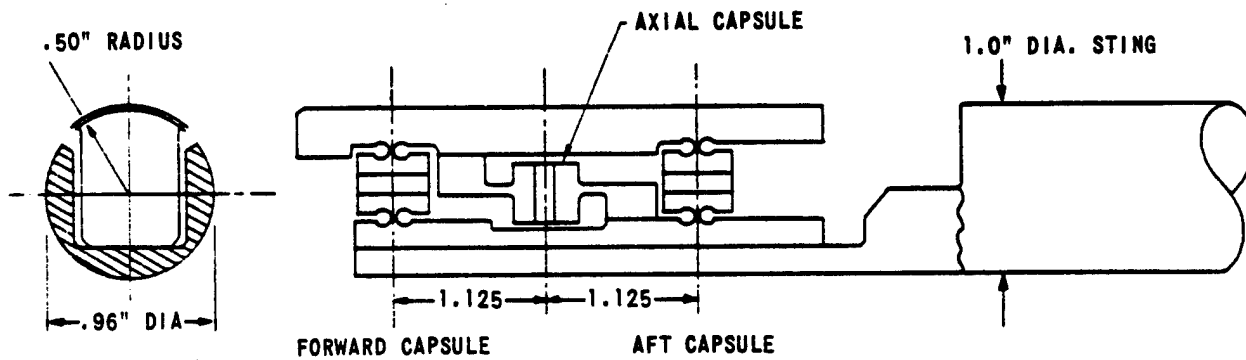
Balance	Balance Diameter (inches)	Number of Components	Maximum Load Per Force Capsule (lbs.)	Maximum Balance Load with 1" C.P. Travel — (lbs.)
F	1.00	3	Normal: 106 Axial: 56	Normal: 150
H	3.125	6	Normal & Side: 64 Axial: 92	Axial: 180
M	1.250	6	Normal & Side: 666 Axial: 100	Normal: 1600

Pure accelerometer balances have also been used<sup>24</sup> to measure forces and moments where: (1) the model size or shape prohibits use of a standard force balance or (2) sting interference is not tolerable. In these cases the model is suspended in the tunnel by a thin wire-spring system.



LOAD CAPACITY (300-PSI CERAMIC STRESS)  
 A<sub>1</sub>, A<sub>2</sub>, A<sub>3</sub> - 92 LB (AXIAL BEAMS)  
 L<sub>1</sub>, L<sub>2</sub>, S - 64 LB (LIFT AND SIDE BEAMS),

6-Component H Balance



LOAD CAPACITY (300 PSI CERAMIC STRESS)  
 AXIAL - 56 LB  
 L<sub>1</sub>, L<sub>2</sub> - 106 LB

3- Component F Balance

Figure 18 Schematic Diagrams of Typical Crystal Balance Systems

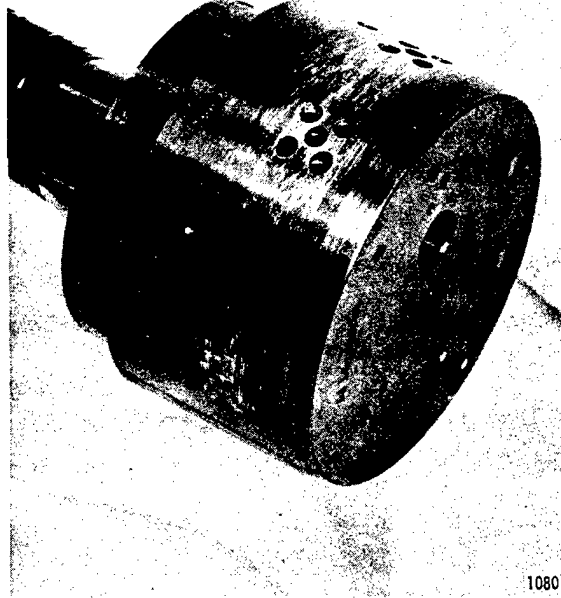
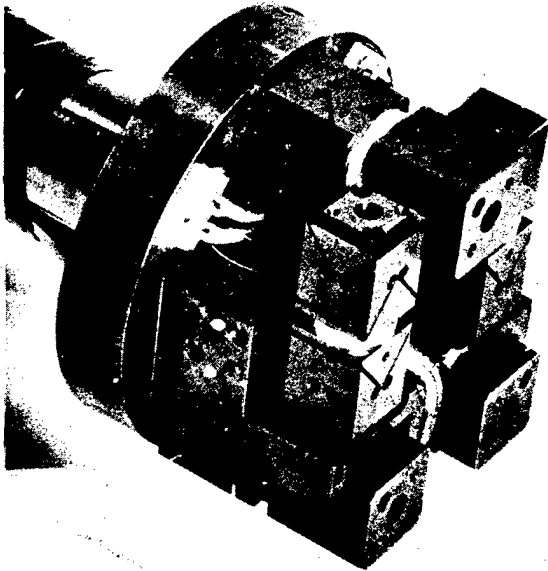
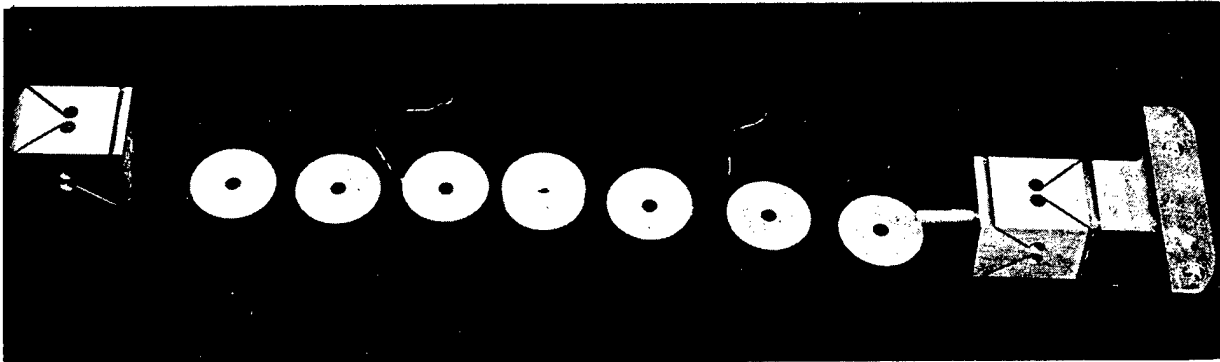


Figure 19 Force Balance Capsule and Balance Assembly

Two analog computers have been designed to meet the specific requirements of the Calspan balance systems. One system is a three-component computer; the other is a six-component computer. A balance is first statically calibrated by hanging a series of weights on the balance and recording the force capsule voltage outputs. Then the model is mounted on the balance and a compensation procedure in which the model undergoes known translational and rotational accelerations about three chosen axes provides the inputs for adjustment of the computer. The computer, by combining the force balance and accelerometer signals, supplies as outputs to the recording system the values for the aerodynamic forces and moments. Once the balance is compensated, a check calibration is made of the complete model balance system to verify the accuracy of the compensation.

### Skin Friction

The skin friction gages<sup>18,25,26</sup> have 0.25-inch diameters and are .375-inches high. These gages use lead zirconium titanate piezoelectric ceramics as the sensing element and field effect transistors (FET) as power amplifiers. Like the pressure transducers described on page 26, the skin friction gages similarly employ a second piezoelectric ceramic and a mass equivalent to the metric diaphragm for acceleration compensation. The floating shear sensitive element (Figure 20) may be flat or contoured and flush mounted so that a smooth surface is presented to the flow. Figure 21 presents some typical skin friction data obtained with these gages on a sharp flat plate.

Two groups of skin friction gages, a high sensitivity type for low density applications and a high load type for turbulent flow, are available. The nominal characteristics of these skin friction gages are as follows:

	High Sensitivity	High Load
Skin friction range ( $\pm 2\%$ linearity and S/N 30)	.0001-.2 psi	.001-2 psi
Relative sensitivity to pressure	1000	1000
Maximum over pressure	50 psia	100 psia
Maximum heat transfer rate	50 BTU/ft <sup>2</sup> sec	200 BTU/ft <sup>2</sup> sec
Low frequency response	1% droop in 100 ms	1% droop in 10 ms
Resonant frequency (approx.)	15,000 cps	15,000 cps
Sensitivity to accel. in direction	$2 \times 10^{-4}$ psi/g	$1 \times 10^3$ psi/g
Diameter of diaphragm	.25-in.	.25-in.
Diaphragm replaceable for contour change	Yes	Yes

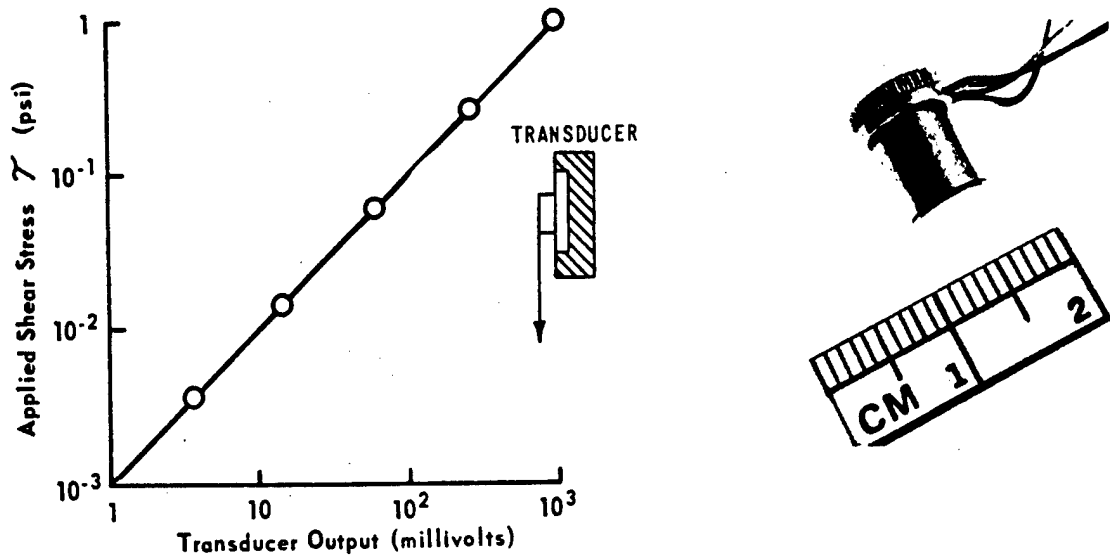


Figure 20 Skin Friction Transducer

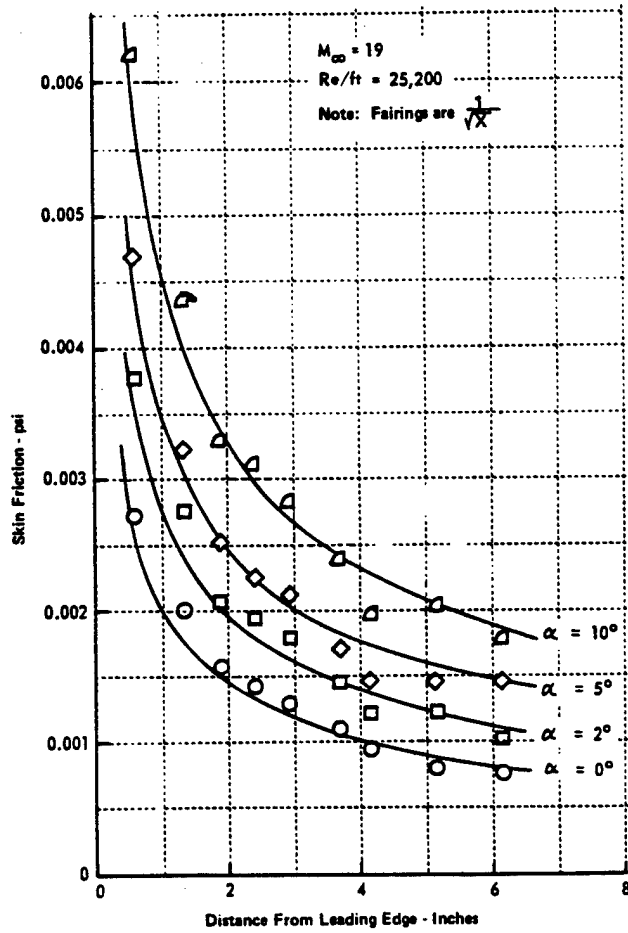


Figure 21 Skin Friction Distribution on a Flat-Plate Model

## The Electron Beam Fluorescence Technique (EBFT)

EBFT<sup>27,31</sup> is a well-established method for investigating rarefied hypersonic flowfields where the number density, is less than about  $10^{16}/\text{cc}$ . Harvey<sup>31</sup> has recently shown that EBFT can also be used at equivalent densities up to over 100 torr. A study using EBFT in a shock tunnel has demonstrated a capability to obtain turbulent fluctuation measurements up to frequencies approaching 1 MHz in hypersonic flows.

Figure 22a, b shows a picture of the equipment used to apply the EBFT in a wind tunnel experiment. Briefly, the EBFT technique involves firing a highly collimated beam of high energy electrons into the test gas flow; the interaction of the electrons with the gas molecules gives rise to optical-band radiation that can be analyzed spectroscopically to obtain estimates of rotational temperature, vibrational temperature or the molecular number density of the excited species. The optimum accelerating voltage for the nitrogen excitation has been found experimentally to be approximately 50 kV. The 50 kV electron beam gun also provides good penetration of the beam through a relatively dense gas.

A picture of the E-beam installation in a sharp-tipped cone configuration is shown in Figure 22a. A compact 50 kV gun is installed within the model and the beam is fired through a small orifice in the surface directly into the cone's boundary layer. A single electro-magnet to focus the beam has been especially designed. It is shaped to fit within the model and yet finely focus the beam at a point coincident with the surface. Here the beam passes through a very small hole in a graphite diaphragm which is shaped to be flush with the model surface. The hole allows the electrons to enter the test flow but effectively isolates the interior of the gun from the external environment. The gun has been ruggedly designed to withstand the shock loading that is inevitable with intermittent wind tunnels. A Farady cup is placed on the electron gun axis outside of the test flow to safely capture the beam and record its current immediately before each test run.

### Gas Sampling and Analysis

Gas sampling equipment has been developed in support of air-breathing propulsion systems and for tunnel-airflow diagnostic purposes.<sup>15</sup> The probe is designed to taking a direct sample of the flowing gas for subsequent measurement of its composition. The probe is closed at the beginning of nozzle airflow, opens at a predetermined time, remains open for 2 milliseconds or less and collects a sufficiently large (6 cc) sample for accurate analysis using standard gas chromatographs or mass spectrometers. The valve is designed to seal before opening (to maintain a vacuum in the probe) and after sampling (to prevent dilution of the sample).

### Laser Holographic System

Holographic interferometry<sup>32</sup> is used extensively in the shock tunnel to examine quantitative and qualitative characteristics of hypersonic flowfields. Holographic interferometry is an important measuring technique, because it is nonintrusive and offers the potential to capture information of the entire flowfield in a single instantaneous exposure.

The holographs of the flowfield are obtained with a pulsed ruby laser that is Q-switched passively with a dye cell to produce single 25-nanosecond (nominal) light pulses. Both single plate and dual plate techniques are used to record holograms, which are subsequently used in the playback step to obtain shadowgrams, schlieren photographs and interferograms of the shock tunnel tests.

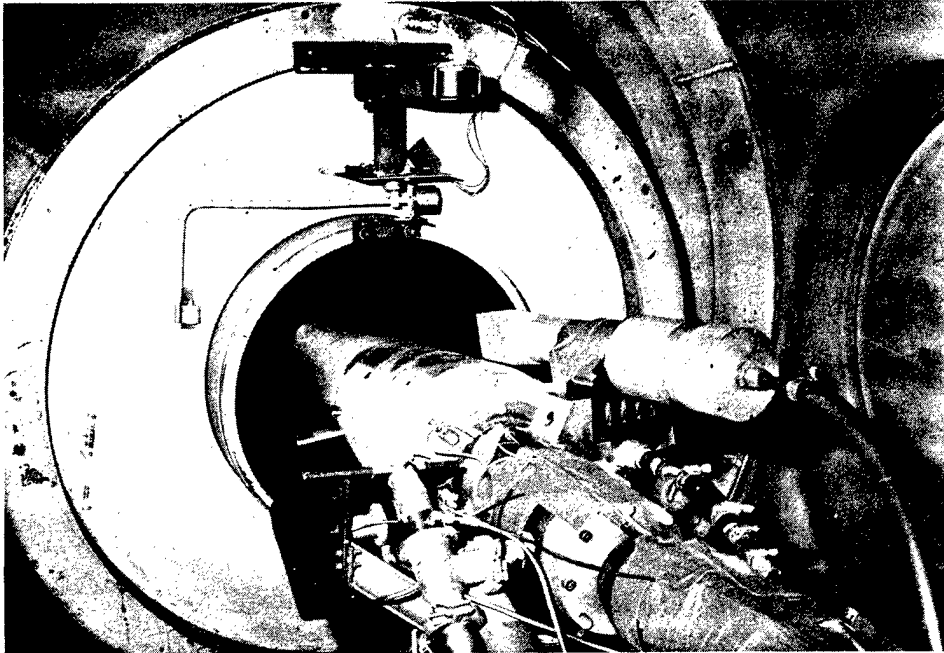


**Figure 22a** INSTALLATION OF OPTICAL DETECTION SYSTEM OF ELECTRON BEAM GUN IN TUNNEL

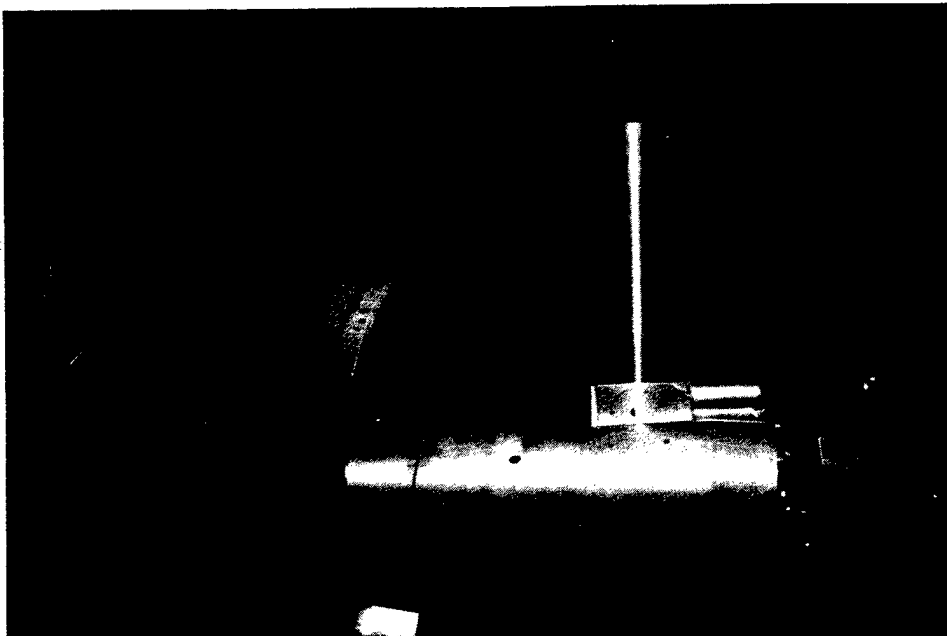


**Figure 22b** ELECTRON BEAM GUN IN OPERATION

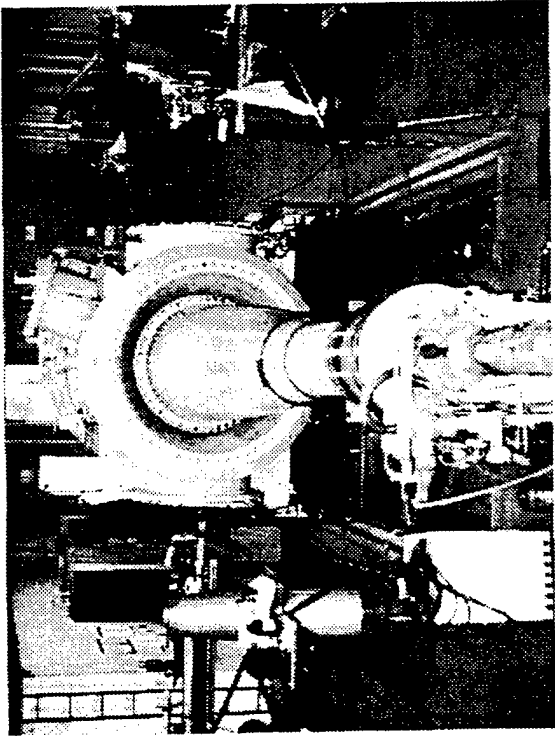
The ruby laser in the recording system is a Korad, single-oscillator system that is passively Q-switched with a Kryptocine dye cell. The bank voltage applied to the flash lamp and the dye concentration in the cell are adjusted so that the laser emits a single pulse energy of 25 milljoules in 25 to 50 nanoseconds, nominally. The output beam has a 0.06-inch diameter at the front reflector of the ruby laser cavity. A typical holographic system is illustrated by Figure 23a.

A separate play-back system is used to measure the interferometric fringe shifts for both single plate and dual plate applications, as well as to obtain photographic enlargements of selected apertures for the flowfields. This latter feature is especially valuable, because it allows details of the flow, which are otherwise invisible, to be observed and studied. Alternatively, a Graflex camera with a 4 x 5 Polaroid film holder is used in place of the microcomparator to photograph the full-aperture views of the flowfields. During hologram playback, the reconstructed light waves converge from the holograms to form a duplication of the true focus of the second parabolic reflector in the recording system, permitting schlieren studies to be accomplished. Figure 23b shows a typical interferogram of the separated turbulent shock boundary interactions which can be obtained from the holographic system.

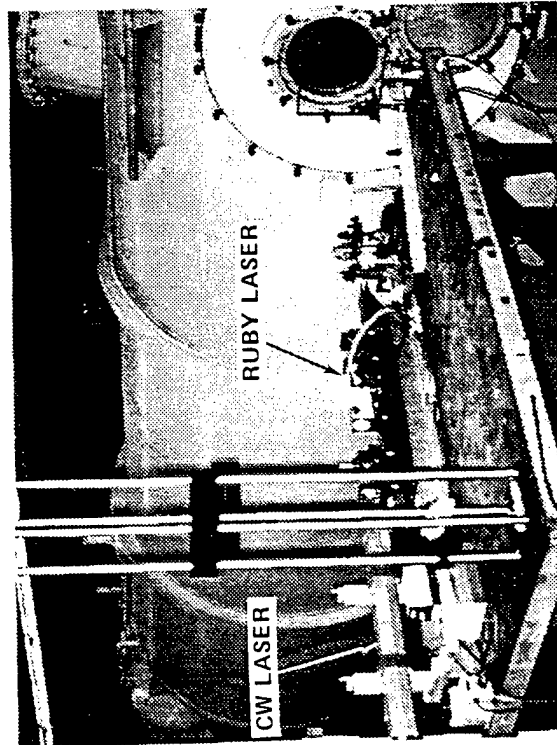
### CFD Validation Studies

Recent intense activities in the development of Computational Fluid Dynamics (CFD) techniques have resulted in significant development in formulating efficient and stable numerical algorithms. However, before its full potential can be realized, a measure of confidence must be established regarding its ability to predict complex flowfield situations. Confidence in computational methodology has been typically achieved by comparison with experiment and this process is referred to as "code validation".

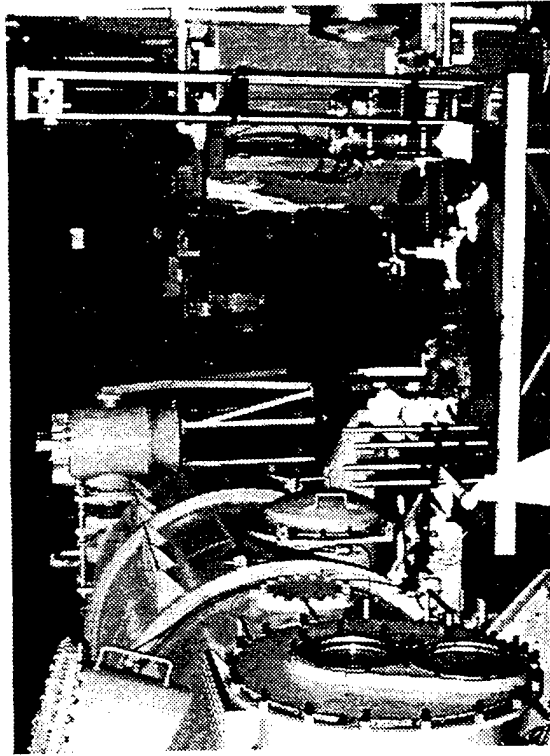
Hypersonic laminar viscous-inviscid interaction problems simulated in the shock tunnels have been used by Rudy et al.<sup>33</sup> as the test cases for validation of the state-of-the-art CFD codes. Typical comparisons of skin frictions, wall pressure, and heat transfer rate measurements taken with the instrumentations described earlier to the CFD predictions are given in Figure 24. Figure 25 is the Schlieren photographs of flowfield of the test cases considered.



96-INCH HYPERSONIC SHOCK TUNNEL WITH LASER HOLOGRAPHIC SYSTEM INSTALLED



SENDING OPTICS



RECEIVING OPTICS

Figure 23a LASER HOLOGRAPHIC SYSTEM



Figure 23b FLOW STRUCTURE IN A TWO DIMENSIONAL CORNER FLOW ( $M=11$   $Re_L = 30 \times 10^6$ )

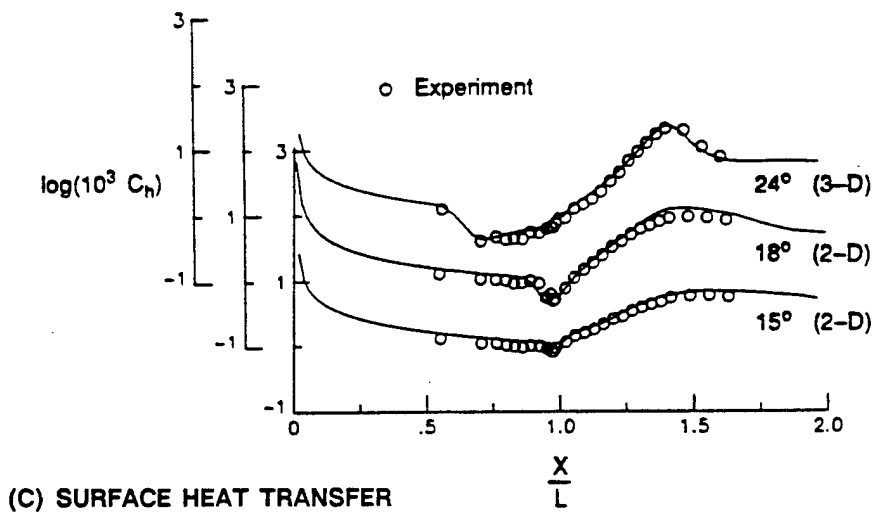
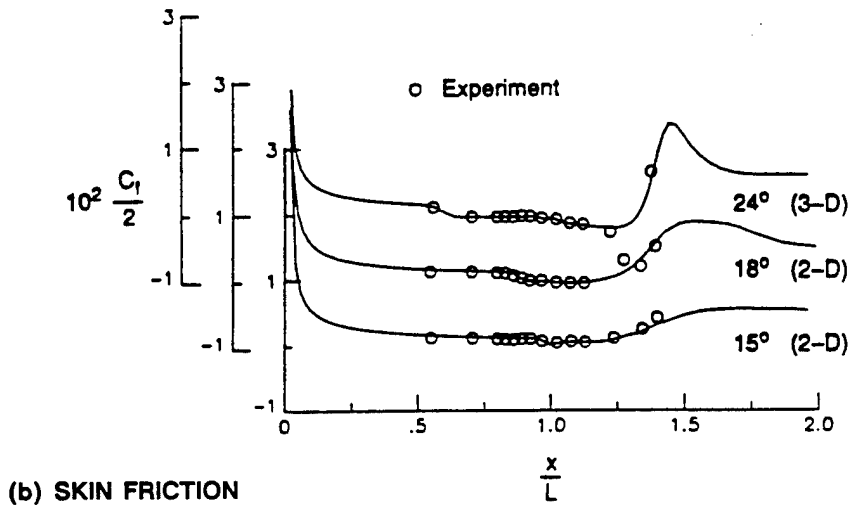
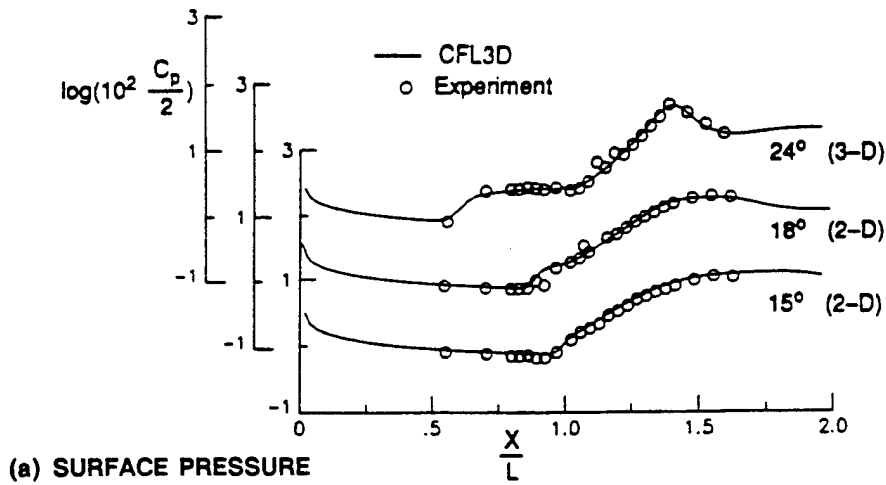


Figure 24 SUMMARY COMPARISON OF COMPUTATIONS WITH EXPERIMENTAL DATA OF MACH 14 FLAT PLATE - WEDGE SHOCK WAVE BOUNDARY LAYER INTERACTION

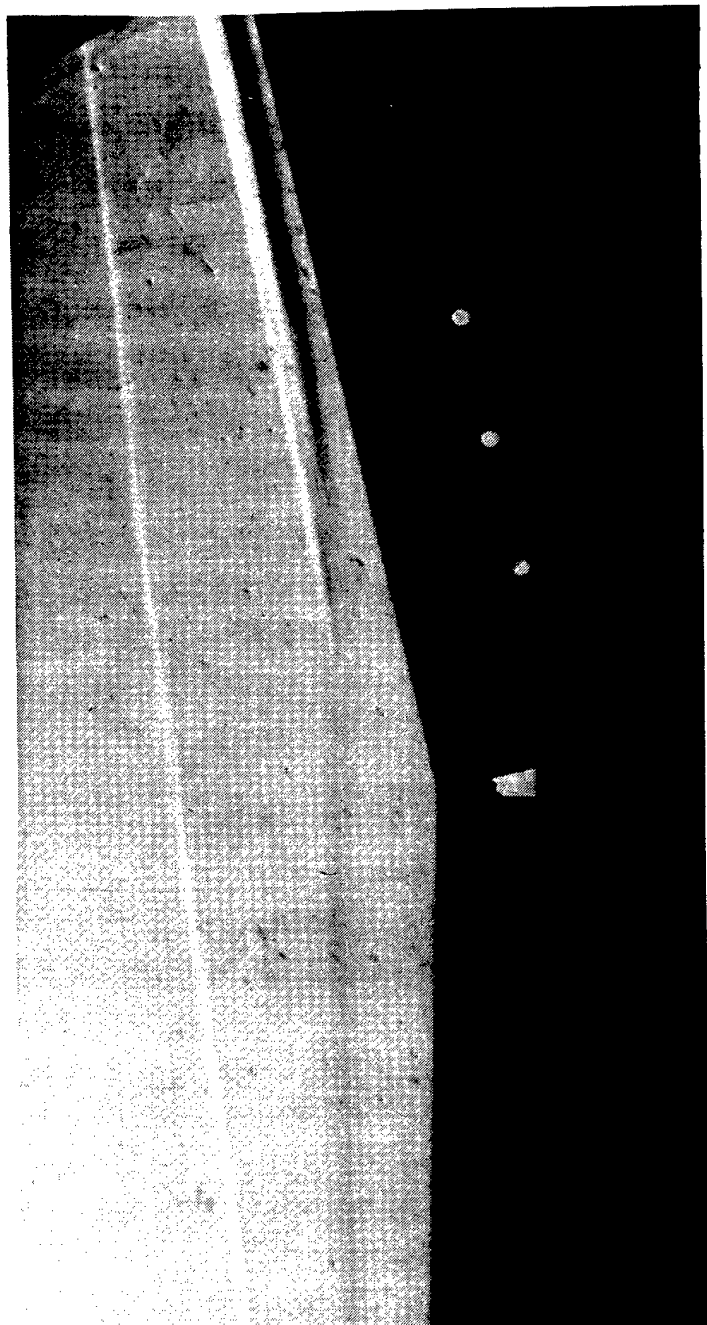


Figure 25 SCHLIEREN PHOTOGRAPH OF MACH 14 TWO DIMENSIONAL  
LAMINAR CORNER FLOW

## AERO-OPTICAL MEASUREMENTS OF SEEKER HEAD PERFORMANCE\*

The optical performance of a seeker head aperture will be based on the refraction and radiative environment introduced by the flow over the seeker head. Non-uniform and turbulent flows over the seeker head induce refractive effects which degrade the optical performance of the IR seeker; also, radiative emission from high temperature air and coolants will reach the IR focal planes raising background levels and degrading performance. The optical evaluation of seeker head apertures will be based on direct measurements of refractive and radiative levels produced in the flow.

The refractive degradations will be measured with a combination of wavefront distortion and image formation diagnostics. The wavefront distortion produced by the flow over the seeker head will be measured directly with holographic interferometry (HI). Pulsed laser holography is a practical and accurate means for interferometric measurements of wavefront distortion. With the attendant specification of the seeker aperture and wavelength, the focal plane intensity distribution is obtained through Fourier analysis. The image formation approach has the advantage of producing a real image (i.e., with actual lens elements) and recording real intensity distributions. This bypasses the rather complex step used in HI of high-resolution phase measurements and two-dimensional Fourier transform. The distinct disadvantage is that the optical degradation is wavelength and aperture dependent and therefore this evaluation is less comprehensive than the HI diagnostic. The HI diagnostic provides direct wavefront distortion measurements and through analysis provides image blur, MTF, PSF data for the wavelength and aperture size of interest. The imagery diagnostic provides direct measurement of BSE, jitter image blur, MTF and PSF.

The radiative environment achieved in the high temperature flow over the seeker head produces an increased background level on the focal plane and absorbs incident target radiation. Several lines of sight will be viewed with radiometers which will sense band radiation in the UV, visible, near, mid and far infrared spectral regions. These radiation levels are expected to depend on incident gas velocity and density, coolant gas and seeker head design.

The performance evaluation of the seeker head aperture will be based on the optical (refractive) quality and the transmission (radiance) properties achieved in the flowfield.

### Aero-Optics Measurement System

The aero-optic diagnostic system will characterize the optical degradation produced by the air and coolant flows over the seeker head aperture. The optical wavefront distortion blurs, shifts and jitters the target image on the focal plane sensor, thus degrading line of sight data to the guidance and control system. The current state-of-the-art instrumentation for characterization of optical degradation includes direct wavefront measurements with holographic interferometry and point-source imagery.

---

\*Dr. James Craig of SRI is assembling and validating the aero-optical instrumentation which will be used in the evaluation of aperture performance. Information directly related to the performance of this system can be obtained directly from Dr. Craig by calling 714-727-1895.

### A. Holographic Interferometry

Aero-optic holographic interferometry (HI) provides visual and quantitative measurements of the optical effects of coolant turbulence. Direct measurement of optical wavefront distortion is achieved through interference with a plane optical wave. In its most simple form, HI is accomplished by recording both the plane (flow-off) and the distorted (flow-on) wavefronts on the same holographic plate. When reconstructed, such holograms reproduce both wavefronts on the same holographic plate. When reconstructed, such holograms reproduce both wavefronts, and the resulting interference depicts the flow-on wavefront distortion. Vibration is tolerated between these steps by recording the plane and distorted waves on separate holograms, and through the incorporation of a double-plate hologram reconstruction device, which superimposes the two waves. In reconstruction the relative hologram positions are adjusted to achieve either the infinite or the finite fringe configuration. The interference fringes depict the changes produced by the flow, which in the case of heated flow wind tunnels can also include thermal distortions. This approach is known as single pulse holographic interferometry (SPHI) since only one flow-on exposure is used.

In double-exposure or double-pulse HI (DPHI), two holograms are superimposed in rapid succession in the recording step on a single plate or film. Since both holograms are recorded in the presence of flow, the interferogram fringes depict the change in the turbulence induced distortion between the pulses, which complicate the interpretation of the interferogram. However, the fact that each pulse traverses a turbulent volume possessing stationary statistics in time is the basis for the quantitative interferometric analysis. Since the mean flow in which the turbulence is embedded is steady in time, the turbulence statistics such as velocity and density correlations are time invariant. Hence for optical waves which traverse such media the spatial statistics of the distortion are also time invariant. The RMS distortion of the difference wavefront is obtained by interferometric analysis. If a statistical set of DPHI's are analyzed, then the statistical average of the RMS is related to that of the absolute phase.

As shown in Figure 26a, the SPHI's fringes exhibit both the slow curvature from the hot facility windows or from imperfectly cooled seeker head windows and the high frequency distortions induced by turbulence, whereas the DPHI's fringes exhibit only the effects of the turbulence. The analysis of the single and double pulse HI's are different because the wavefront or phase map depicted in the SPHI can be directly propagated to the focal plane, but the differential wavefront depicted in the DPHI can only be utilized to obtain phase statistics. The focal plane intensity distribution, or more appropriately, the point spread function (PSF) is uniquely dependent on the wavefront distortion or phase map (i.e., obtained from SPHI's) through Fourier or diffraction analysis; or as an alternative, the PSF is also related to statistics of the wavefront distortion, namely the RMS and integral length scale. These wavefront or phase statistics can be obtained through analysis of the DPHIs. Hence, both the phase map and the phase statistics are measured.

#### Phase Measurement

The phase map is measured with HI through conventional fringe tracing methods and advanced interferometry methods (Figure 26b), which offer increased spatial resolution and accuracy. Fringe tracking interferometry is a phase measurement technique in which the fringe centers are identified as contours of constant phase. After a plane wave is fit to the interferogram phase contours, the phase is determined along straight lines through the fringes. This is phase measurement through finite fringe interferometry. Now if a continuous, 2-D phase map is desired, the space between the fringes must be filled by interpola-

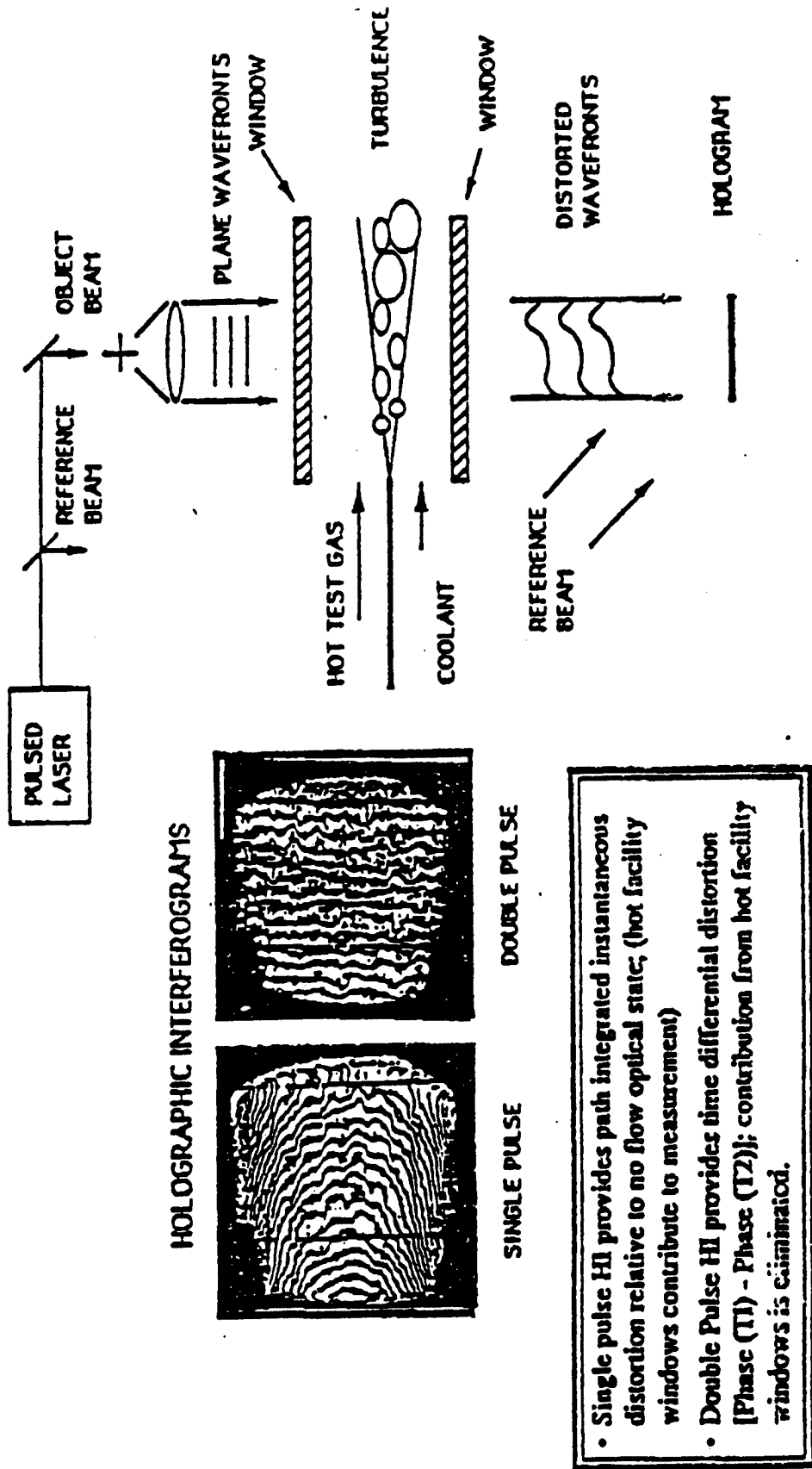


Figure 26a SINGLE AND DOUBLE PULSE HOLOGRAPHIC INTERFEROMETRY

	Single-Pulse	Double-Pulse
Fringe Tracking	Does not provide phase data between fringes	Provides accurate phase correlation function along fringes  Record DPHIs with fringes in both directions
Phase-shifting Interferometry	Provides high accuracy. Performs noise rejection. Provides "filled in" phase maps Provides high spatial resolution	Difficult to implement with conventional hologram recording.
Fourier Transform	Provides "filled in" phase map	Provides same data as Fringe Tracking

**Figure 26b PHASE MEASUREMENT FROM HOLOGRAPHIC INTERFEROGRAMS**

tion. If the phase map contains high spatial frequency turbulence in a direction normal to the fringes, then interpolation is not satisfactory. However, the fringe tracking does provide high resolution phase statistics in the direction parallel to the fringes. The information obtained along the fringes provides an excellent measurement of the phase statistics. In fact, the phase correlation function along the fringes is determined directly and provides both the RMS and the integral length scale. Since the fringes in the DPHIs can be oriented in either cross aperture direction, the integral scale can be measured in both directions.

Phase-Shifting Interferometry (PSI) and Fourier Transform (FT) are advanced interferometry are methods which utilize the variation of intensity between the fringes to obtain a higher resolution measurement in the direction normal to the fringes. In contrast to fringe detection algorithms, PSI achieves phase measurement through electronic means. If the relative phase is shifted between the two waves reconstructing the holographic interferogram, then the fringe pattern will be shifted by an associated amount. By shifting the phase by precise amounts, new independent equations are obtained. Three such independent equations provide a solution for the phase. the procedure is to measure the three intensities at every point in the interferogram for three imposed phase shifts, and then to obtain the phase map. The method resolves the high spatial frequency phase distortions through the use of a high resolution CCD camera.

The fourier Transform (FT) method of phase measurement is ideally suited for DPHIs in which the fringes are relatively straight except for the high frequency distortion. The desired phase map is separated from the noise and is extracted by filtering in the frequency plane. The phase map is obtained from alogarithmic relationship. A uniformly sampled phase map is obtained across the aperture. Since this is a differential phase map, the RMS phase distortion and the integral length are obtained in both the flow and cross-flow directions within the aperture.

#### Point Spread Function

The phase map is scaled longer or shorter wavelength (Figure 26c). For example, at 2.0 um the phase distortion is 0.08 waves and at 0.3 um the phase distortion is 0.5 waves. When these wavefronts are propagated to the Fourier transform plane, one observes major differences in the intensity distribution. At the longer wavelength, 2.0 um where the phase distortion is weak, the image formation is nearly diffrac-

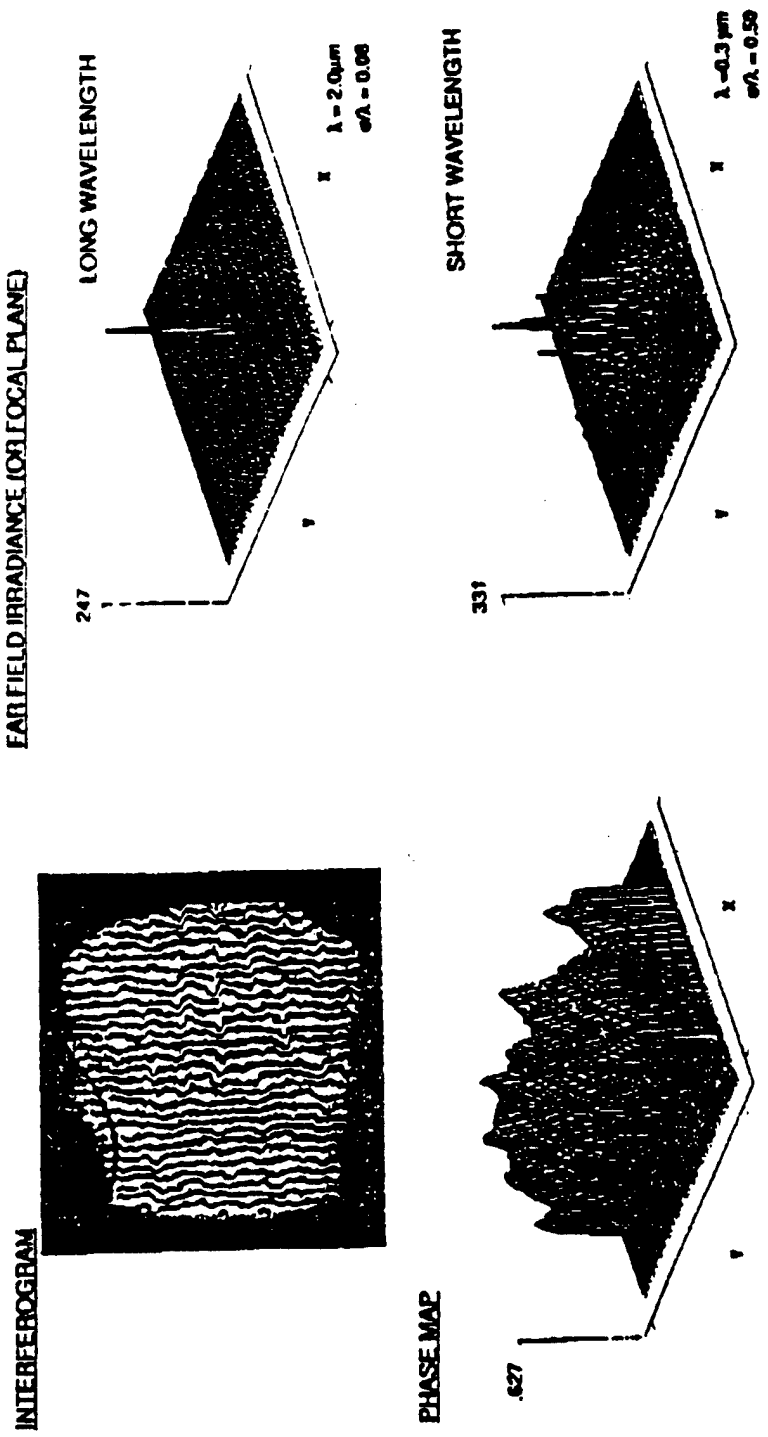


Figure 26c SEEKER FOCAL PLANE ANALYSIS FROM INTERFEROGRAM

tion limited as shown by the singular spike in the center of the focal plane. Conversely, at the shorter wavelength, 0.3  $\mu\text{m}$ , where the phase distortion is strong (i.e., more characteristics of levels expected for ENDO LEAP sensors), the image formation process results in an intensity distribution characterized by multiple spikes with the light spread over a larger portion of the focal plan array.

### *B. Visible Imagery*

A visible wavelength imagery system is an integral component of the aero-optics instrumentation. The imager field-of-view is co-axial with the holography system and operates simultaneously. A pulsed light source is used and a telescope will be used to form the source image on the detector array. Various forms of one- and two-dimensional scanning are implemented to expose a large number of images during the short duration flow. A focal plane will be used to obtain the required intensity distribution accuracy and resolution. Further, we will utilize a wideband/dynamic range video digitizer to record the CCD exposures. The imager also implements a line of sight detector for SBE/jitter measurement.

The aero-optic measurements of refractive degradations includes wavefront distortion levels and scale size; point spread functions measured at one wavelength (imagery) and computed from holography data at several other wavelengths, and mean and fluctuating (jitter) bore-sight error. The wavefront distortion of phase maps are also analyzed as modulation transfer functions which are of more general use to sensor designers.

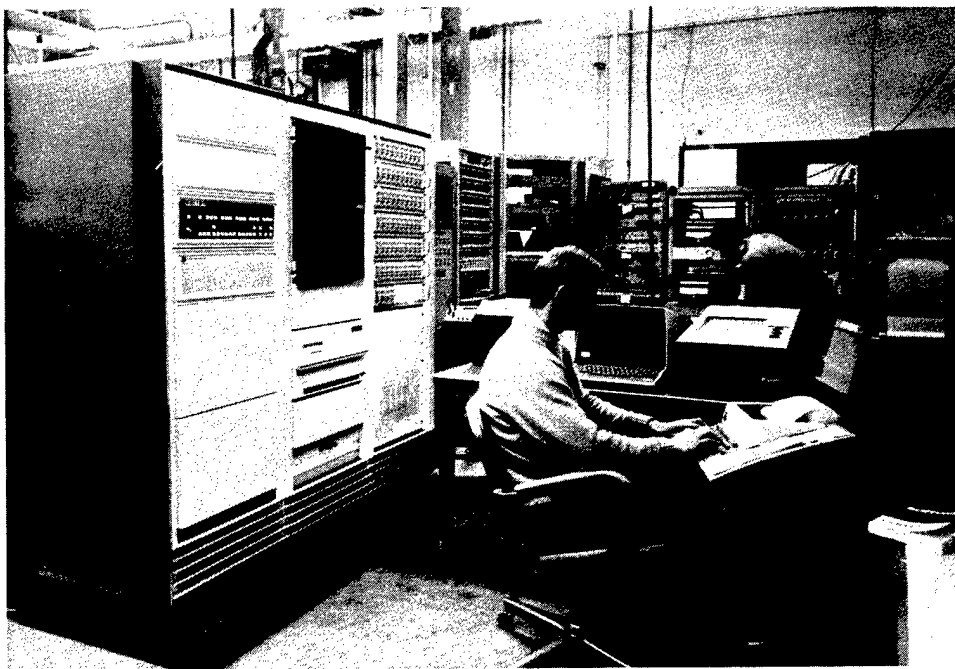
## DATA ACQUISITION AND PROCESSING SYSTEM

All data are recorded on a 128-channel Calspan Digital Data Acquisition System II (DDAS II). This system consists of 128 Marel Co. Model 117-22 amplifiers, an Analogic ANDS 5400 data acquisition and distribution system and a SUN 4/75GX computer. The Analogic system functions as a transient event recorder in that it acquires, digitizes and stores the data in real time. Immediately after each test run the data is transferred to the SUN computer for processing. An additional 108 channels are available through Calspan's Digital Data Acquisition System (DDAS I) and 32 channels high frequency (3 MHz sample rate) response Data Lab transient recorder.

The Marel amplifiers provide gains up to 1000 for low-level signals, can be AC or DC coupled to the transducers, and have selectable low-pass filters with cut-off frequencies of 300, 1000 or 3000 Hz. The Analogic system contains a sample-and-hold amplifier, a 12-bit analog-to-digit converter and 4096 sample memory for each channel.

After the data are transferred to the SUN computer, plots of the analog voltage time histories are generated to determine the overall quality of the data and to select the steady-flow time interval. The data are then reduced to engineering units, i.e., psi or °F and, in the case of pressures and temperature, averaged over the selected steady-flow time interval.

The raw data (voltage) time histories are transferred to a Hewlett Packard 9-Track tape drive for archival storage while temporary storage of raw and reduced data is on a 1.2 GByte disk drive of the SUN computer. Standard 3 $\frac{1}{2}$  and 5 $\frac{1}{4}$  disk drive subsystems also permit downloading of reduced data files for transfer of data to microcomputers. Two NCD X-terminals are interfaced to the SUN, in addition to the system's main terminal, allowing multi-user access supporting data reduction, analysis and reporting functions. Tabulations and time history plots of raw and/or reduced data are generated using a QMS Image Station printer.

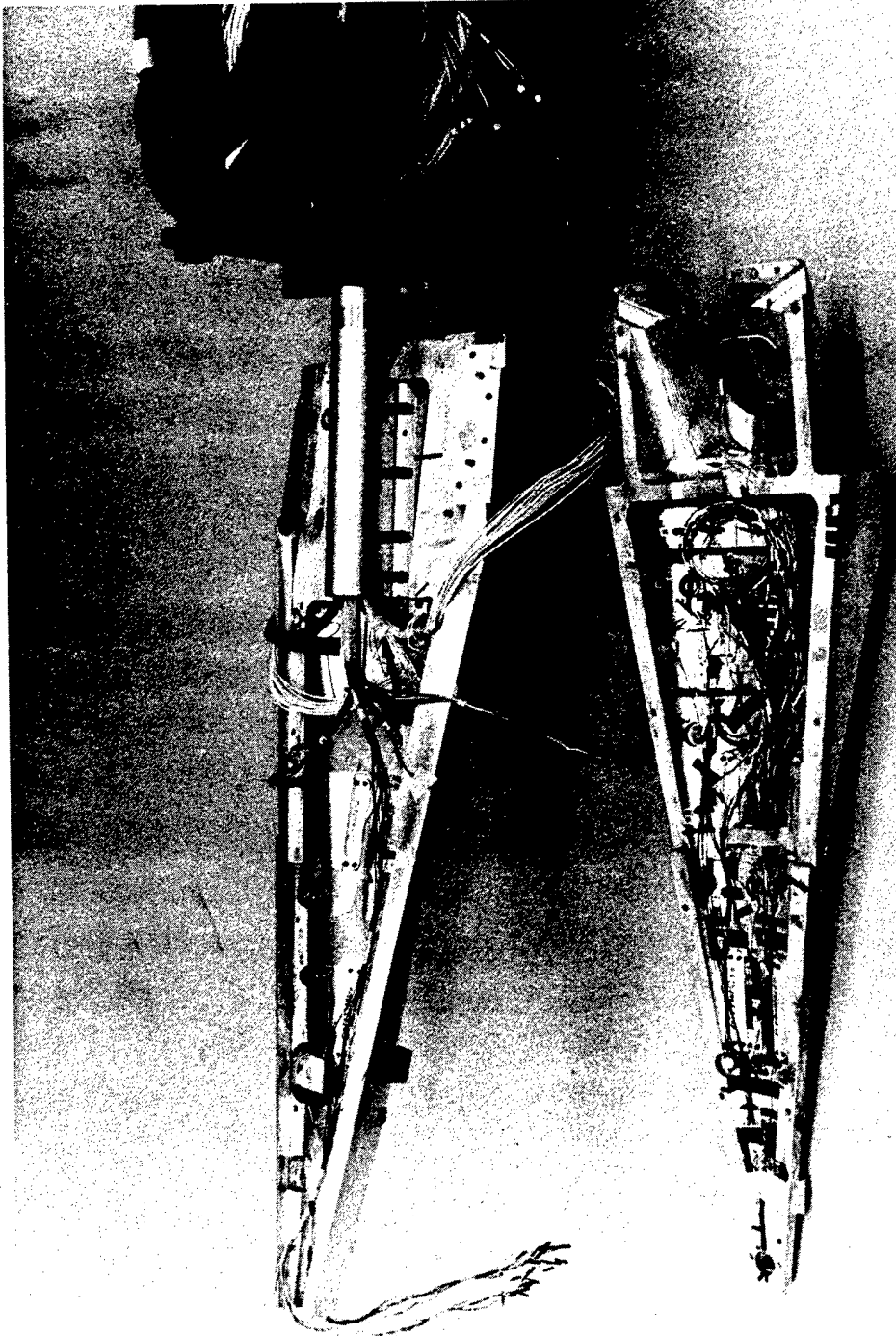


## MODEL DESIGN AND FABRICATION

Generally it is advisable to have the models designed, fabricated, and instrumented in consultation with the CUBRC staff. CUBRC has broad experience and capability in the design of wind tunnel models, complex instrumentation, special sting mounts, and 3- and 6-component force and moment balances. Specialized instrumentation can also designed and fabricated for the contractor; the contouring of sensors, such as heat-transfer and skin-friction gages, to model surfaces is a fairly standard procedure.

On all customer-furnished models a complete stress analysis is required prior to testing. Generally, a safety factor of 5 must be shown on all components. It is recommended that on any customer-furnished models, drawings be submitted to the shock tunnel staff for approval prior to the start of fabrication.





INSTRUMENTATION OF HYPERSONIC VEHICLE CONCEPT

## MODEL SUPPORT AND OPTICAL BENCH SYSTEMS

In the LENS facility, as in the 48- and 96-inch tunnels at Calspan, the model support system is mechanically isolated from the test section. The base of the model support system is bolted to the ground through the isolation mounting and sealed to the tunnel with "Bellophragms"—a rolling diaphragm which transmits virtually no force. The test section and the driver and driven tubes are attached to rollers through isolation blocks. The rollers, which run on rails bolted to the ground, allow free movement of the test section independent of the model support system. Two types of support system can be mounted on the model support base. The sting and sector system shown in Figure 27 provides the capability to mount models from the rear and is used extensively for flight vehicle tests. Figure 28 shows a customized mounting from the base plate which is a potential configuration which houses the optical benches which would be used in the initial aero-optic validation tests to be conducted in the LENS facility. The optical bench is housed within the model support system which is itself shielded from aerodynamic forces by fairing which are attached to the tunnel. A key advantage of the short test time is that low frequency isolated systems can be designed which effectively prevent facility loads being transmitted to the model and optical benches until long after the test time of the tunnel.

The load limits for the sting mounting system are shown below

Tunnel	Angle of Attack Range deg	Angle of Attack Increments deg	Allowable Maximum Moment in. lb.	Equivalent Load at Center of Rotation lb.
48I Log Standard Sector High Load Sector	0 to +53.5 0 to 40	Continuous 5	35,200 —	800 6000
LENS	0 to 50	Continuous	800,000	10,000

In defining these load limits, it is assumed that all model loads are subject to dynamic overload factors of 2.0. These limits are offered only as a guide and loading and stressing data must be supplied to CUBRC to validate the integrity of the system.

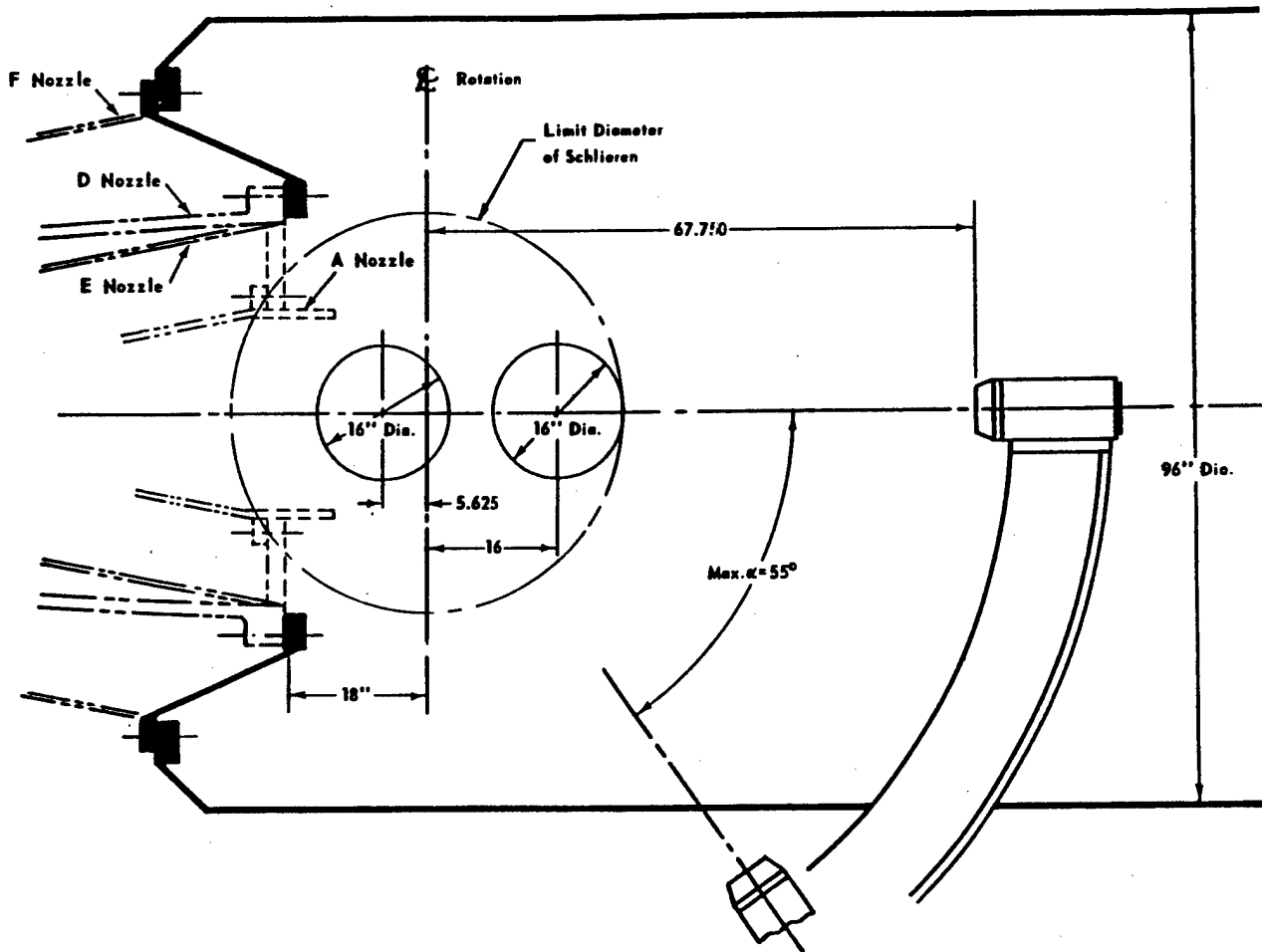


Figure 27 LENS MODEL SUPPORT

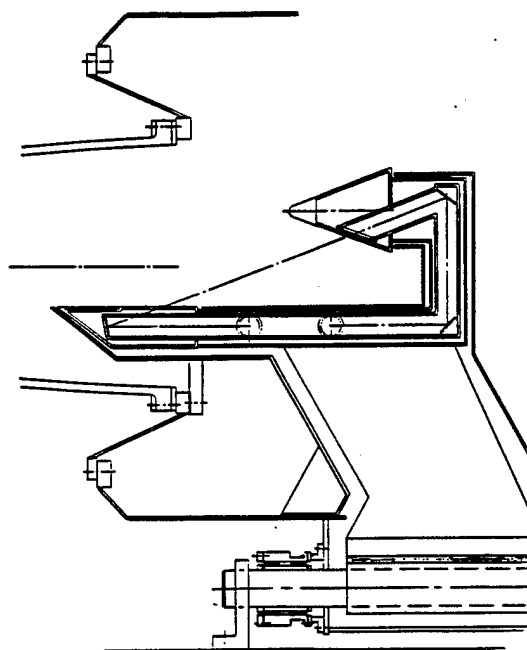


Figure 28 MODEL AND SOURCE INSTALLATION FOR AERO-OPTIC STUDIES

## REFERENCES

1. Bird, K.C., and Burke, A.F., "The Use of Conical and Contoured Expansion Nozzles in Hypervelocity Facilities," Calspan Report No. 112, January 1962.
2. Daum, Fred L., "Air Condensation in a Hypersonic Wind Tunnel," AIAA Journal, Vol. 1, No. 5, May 1963.
3. Griffith, B.J., Deskins, H.E., and Little, H.R., "Condensation Tests in Hotshot Tunnels," Third Hypervelocity Technique Symposium, March 17-18, 1964.
4. Reece, J.W., "Shock Tube Theory for Real Air with Application to Wind Tunnel Testing and to Flight Simulation," Calspan Experimental Facilities division report WTH-003, October 1958.
5. Boyer, D.W., Eschenroeder, A.Q., and Russo, A.L., "Approximate Solutions for Nonequilibrium Air Flow in Hypersonic Nozzles," Report No. AEDC-TN-60-181, August 1960.
6. \* Burke, A.F., Curtis, J.T., and Boyer, D.W., "Nonequilibrium Flow Consideration in Hypervelocity Wind Tunnel Testing," Calspan Report No. AA-1632-Y-1, May 1962.
7. Curtis, J.T., Burke, A.F., and Hayman, R.A., "An Analytical and Experimental Study of the Ionized Flowfield about a Hemisphere Cylinder and its Effect on the Radiation Pattern of a Slot Antenna," Report No. AFCRL-63-339, August 1963.
8. Andre, S.N., "Study of Antenna Voltage Breakdown in a Shock Tunnel," Final Technical Report AFCRL-68-0253 (Calspan Report No. UB-2344-E-4), January 1967-April 1968 CONFIDENTIAL.
9. Boyer, D.W., "Ionization Nonequilibrium Effects on a Magneto-gasdynamics Interaction on the Stagnation Region of an Axisymmetric Blunt Body," Report No. ASD-TDR-62-1078, March 1963.
10. Garberoglio, J.E., Dukowicz, J.K., and Romeo, D.J., "Experimental Investigation of Turbulent Near Wakes in Hypersonic Flow," Calspan Report No. WTH-032, January 1968.
11. Rogers, C.E., and Mason, R.P., "Some Recent Advances in Short-Duration Aerodynamic Testing Techniques," presented at The Second AIAA Aerodynamic Testing Conference, Los Angeles, CA, September 1966.
12. Young, M.C., and Tripp, B.R., "Short-Pulse Coherent Doppler Radar Measurements of Backscatter from Hypersonic Wakes," Calspan Report No. 162, January 1968.
13. Wallance, J.E., and Duryea, G.R., Jr., "Porous Leading Edge Development and Experiments on Transpiration Effects for a Blunt Plate in Hypersonic, Laminar Flow," AFFDL-TR-66-33, Vol. III, September 1966.
14. Burke, A.F., "Turbulent Boundary Layers on Highly Cooled Surface at High Mach Numbers," Calspan Report No. 118, November 1961.

15. Bird, K.D., Martin, J.F., and Bell, T.J., "Recent Developments in the Use of the Hypersonic Shock Tunnel as a Research and Development Facility," presented at the Third Hypervelocity Techniques Symposium, Denver, CO, March 1964.
16. Beal, J.L. et al., "Review Report on CAL Studies of the Breakup of Drops During Reentry," Calspan Report No. AA-2121-Y, March 1967.
17. Martin, J.F., Duryea, G.R., and Stevenson, L.M., "Instrumentation for Force and Pressure Measurements in a Hypersonic Shock Tunnel," Calspan Report No. 113, January 1962.
18. Bogdan, L., "Instrumentation Techniques for Short-Duration Test Facilities," Calspan Report No. WTH-030, March 1967.
19. MacArthur, R.C. and Martin, J.F., "Use of Field Effect Transistors in Shock Tunnel Instrumentation Circuits," Proceedings of the 2nd International Congress on Instrumentation in Aerospace Simulation Facilities, Stanford University, Stanford, CA, 29-31 August 1966.
20. MacArthur, R.C., "The Development of High Output Miniaturized Pressure Transducers for Shock Tunnel Testing," AFAPL-TR-68-37, April 1968.
21. Vidal, R.J., "Transient Surface Temperature Measurements," Calspan Report No. 114, March 1962.
22. Bogdan, L., "High-Temperature, Thin-Film Resistance Thermometers for Heat Transfer Measurements," Calspan Report No. HM-1510-Y-6, February 1963.
23. Rogers, C.E., Bogdan, L., Kinzly, R.E., and Stratton, J.E., "A Thermal Mapping Technique for Shock Tunnels and a Practical Data-Reduction Procedure," AIAA 7th Aerodynamic Testing Conference, Palo Alto, CA, September 13-15, 1972 (AIAA Paper No. 720-1031).
24. Sheeran, W.J., and Duryea, G.R., "The Application of the Accelerometer Force Balance in Short-Duration Testing," presented at the AIAA 4th Aerodynamic Testing Conference, Cincinnati, OH, April 28-30, 1969 (AIAA Paper No. 69-351).
25. MacArthur, R.C., "Transducer for Direct Measurement of Skin Friction in a Hypersonic Shock Tunnel," Calspan Report No. 129, August 1963.
26. MacArthur, R.C., "Contoured Skin Friction Transducers," Calspan Report No. AN-2403-Y-1, August 1967.
27. Wallace, J.E., "Hypersonic Boundary Layer Measurements Using an Electron Beam," Calspan Report No. AN-2112-Y-1, August 1968.
28. Holden, M.S., "Shock Wave-Turbulent Boundary Layer Interaction in Hypersonic Flow," AIAA Paper No. 72-74, paper presented at the AIAA 10th Aerospace Science Meeting, San Diego, CA, 17-19 January 1972.
29. Holden, M.S., "Shock Wave-Turbulent Boundary Layer Interaction in Hypersonic Flow," Calspan Report No. AI-2920-A-1, July 1973.

30. Holden, M.S., "A Preliminary Experimental Study of the Turbulent Near Wake in High Reynolds Number Hypersonic Flow," Calspan Report No. AB-5211-A-1, January 1973.
31. Harvey J., Bergnan, R.C., and Holden, M.S., "An Experimental Study of Hypersonic Turbulence on a Sharp Cone," AIAA Paper No. 89-1866.
32. Havener, G., Holden, M.S., and Azevedo, D., "Preliminary Application of Holographic Interferometry to Study Hypersonic Regions of Shock Wave/Boundary Layer Interactions," AIAA Paper No. 87-1194.
33. Rudy D.H., Thomas, J.L., Kumar, A., and Gnoffo, P.A., "A Validation Study of Four Navier-Stokes Codes for High Speed Flows," AIAA Paper No. 89-1838.
34. Holden, M.S., Nowak, R.J., Olsen, G.C., and Rodriguez, K.M., "Experimental Studies of Shock Wave/Wall Jet Interaction in Hypersonic Flow," AIAA Paper No. 90-0607.
35. Seymour, P.J., "Techniques for Evaluation of Unsteady Heat Flux From Film Gages," Master of Science Thesis at University of Buffalo, 1982.
36. Wittliff, C.E., "Hypersonic Shock Tunnel Heat Transfer Tests of the Space Shuttle SILTS Pod Configuration," AIAA Paper No. 83-1535.
37. Pate, S.R., Schueler, C.J., "An Investigation of Radiated Aerodynamic Noise Effects on Boundary-Layer Transition in Supersonic and Hypersonic Wind Tunnels," AIAA Paper No. 68-375.
38. Stainback, P.C., Fisher, M.C., Wagner, R.D., "Effects of Wind Tunnel Disturbance on Hypersonic Boundary-Layer Transition," AIAA Paper No. 72-181.
39. Watkins, W., "Comparisons of a Full Navier-Stokes Computational Model with High Mach Number Combustor Test Data," AIAA Paper No. 90-5217.